



**HAL**  
open science

## Adaptive Eulerian framework for boiling and evaporation

Mehdi Khalloufi, Rudy Valette, Elie Hachem

► **To cite this version:**

Mehdi Khalloufi, Rudy Valette, Elie Hachem. Adaptive Eulerian framework for boiling and evaporation. Journal of Computational Physics, 2020, 401, pp.109030. <10.1016/j.jcp.2019.109030>. <hal-02422190>

**HAL Id: hal-02422190**

**<https://minesparis-psl.hal.science/hal-02422190v1>**

Submitted on 21 Dec 2021

HAL is a multi-disciplinary open access archive for the deposit and dissemination of scientific research documents, whether they are published or not. The documents may come from teaching and research institutions in France or abroad, or from public or private research centers.

L'archive ouverte pluridisciplinaire HAL, est destinée au dépôt et à la diffusion de documents scientifiques de niveau recherche, publiés ou non, émanant des établissements d'enseignement et de recherche français ou étrangers, des laboratoires publics ou privés.



Distributed under a Creative Commons CC BY-NC 4.0 - Attribution - Non-commercial use - International License

# Adaptive Eulerian framework for boiling and evaporation

Mehdi Khalloufi\*, Rudy Valette, Elie Hachem

*<sup>a</sup>MINES ParisTech, PSL - Research University, CEMEF - Centre for material forming, CNRS UMR 7635, CS 10207 rue Claude Daunesse, 06904 Sophia-Antipolis Cedex, France.*

---

## Abstract

We propose in this work an adaptive Eulerian framework for the simulation of both boiling and evaporation phenomena occurring at the interface of a heated 3D solid immersed in a liquid tank. It simultaneously takes into account the gas-liquid phase changes, the vapor formation and their dynamics, and consequently the 3D quenching or cooling of a heated solid. It uses a Level Set method to separate and to track each phase. The phase change is performed using the balance of heat fluxes at the interface without the use of conforming mesh. Instead, the use of an a posteriori error estimate leading to highly stretched anisotropic elements at the interface enables to drastically reduce errors on computed jumps. This avoids the need of interface reconstruction or interpolation procedure. Finally, a Variational Multiscale solver for the Navier-Stokes equations is extended with implicit treatment of the surface tension. A series of 2D and 3D problems are solved to highlight the efficiency and the accuracy of the proposed framework. The cooling of an immersed solid is also presented and shows good agreement with experimental data. To the best of our knowledge, direct numerical simulations of quenching using an Eulerian framework with boiling and evaporation have never been considered.

*Keywords:* Phase change, Multiphase flows, Immersed method, Level Set, Anisotropic mesh adaptation, Stefan problem

---

## 1. INTRODUCTION

2 An accurate and robust simulation of boiling phenomena is still an ongoing challenge. Indeed, the  
3 complexity of boiling lies in the wide range of scales to consider and in the physics involved. From the  
4 nucleation of vapor bubbles to film boiling and bath hydrodynamics, one needs to consider scales from  
5  $\mu m$  to  $m$ . Indeed, in industrial processes, such as quenching of a solid hot metallic part, the variety of  
6 configurations and the complexity of the surrounding flow must also be taken into account as they have  
7 direct impacts on gradients of mechanical properties, microstructure and residual stresses.

---

\* Corresponding author

*Email addresses:* [mehdi.khalloufi@mines-paristech.fr](mailto:mehdi.khalloufi@mines-paristech.fr), [khalloufi.mehdi@gmail.com](mailto:khalloufi.mehdi@gmail.com) (Mehdi Khalloufi),  
[rudy.valette@mines-paristech.fr](mailto:rudy.valette@mines-paristech.fr) (Rudy Valette), [elie.hachem@mines-paristech.fr](mailto:elie.hachem@mines-paristech.fr) (Elie Hachem)

8 The classical well known methods for thermal treatment during the cooling of a solid generally refer  
9 to the use of experimentally deduced heat transfer coefficients. However, these latter are only useful for  
10 a particular configuration in term of geometry, orientation of the surface, range of temperature and flow  
11 motion. Therefore, heat transfer coefficients are not suitable to analyze different industrial processes and  
12 cannot be generalized to all configurations. Only a direct numerical simulation can take into account all the  
13 physics and all the scales involved in boiling.

14 An abundant research has been devoted to the modeling of the boiling and the evaporation phenomena.  
15 The approaches to simulate these phenomena can be summarized into two categories that depend on the  
16 thickness of the interface: sharp interface and diffuse interface. The sharp interface approach considers  
17 the presence of different phases that interact through the interface using boundary conditions. Within this  
18 approach, two methods are commonly used. First, in interface tracking methods, the interface is represented  
19 by a set of nodes. This set of nodes moves accordingly to the interface. This requires particular mesh move-  
20 ments at each iteration and also requires a special treatment of complex topological configurations [1–5].  
21 Alternatively, interface capturing methods consist in a implicit definition of the interface. A volume fraction  
22 (Volume-Of-Fluid) or a signed distance function (Level Set) is convected using a transport equation [6–18].  
23 These methods are popular due to the simplicity of implementation and the fact that complex topology  
24 changes such as the coalescence of bubbles are handled naturally. A literature review of these methods  
25 applied to boiling is given by Kharangate and Mudawar in [19]. Other approaches in the literature can  
26 be mentioned. Phase-field approaches seem promising [20–22]. An order parameter is used to distinguish  
27 different phases and its evolution gives access to the interface location. The interface is assumed to have a  
28 thickness of a few nanometers. However, an equation of state is required for the fluid which introduces com-  
29 plexity from a mathematical and numerical point of view. Furthermore, this approach introduces high-order  
30 differential terms that may be stiff and require innovative discretization techniques. We can also mention  
31 the fluid mixtures approaches [23, 24] considering two compressible phases, where a complete hyperbolic  
32 system is derived using conservation equations for each phase. An equation of state that reproduces the  
33 phase diagram is usually required to close the system.

34 We propose in this work an adaptive Eulerian framework for the simulation of both boiling and evapora-  
35 tion phenomena occurring at the interface of a heated 3D solid immersed in a liquid tank. It was shown that  
36 an adaptive Eulerian framework is very efficient for the simulation multiphase flows [25–28], compressible  
37 and incompressible flows [29] and yield stress fluids [30]. This framework takes into account the gas-liquid  
38 phase changes, the vapor formation and their dynamics, and enables consequently the simulation of 3D  
39 quenching or cooling of a heated solid. A level set method is used to separate and track the different phases.  
40 The phase change is performed using the balance of heat fluxes at the interface without the use of conform-  
41 ing mesh. Instead, the use of an a posteriori error estimate [31–33] leading to highly stretched anisotropic  
42 elements at the interface enables to drastically reduce errors on computed jumps. This avoids the need

43 of interface reconstruction or interpolation procedure. We derive the Navier-Stokes equations taking into  
 44 account the mass and energy transfer between phases at the interface. A series of 2D and 3D problems are  
 45 solved to highlight the efficiency and the accuracy of the proposed framework. The cooling of an immersed  
 46 solid is also presented and shows good agreement with experimental data. To the best of our knowledge,  
 47 direct numerical simulations of quenching using an Eulerian framework with boiling and evaporation have  
 48 never been considered.

49 The paper is structured as follows. In Section 2, we present the governing equations for the fluid motion  
 50 and the level set transport equation. In Section 3, we recall the main steps of the anisotropic mesh adaptation  
 51 procedure governed by the length distribution tensor. In Section 4, we provide some numerical results and  
 52 examples to assess the capability of the proposed method.

## 53 2. Eulerian framework

54 This section is devoted to the presentation of the Eulerian framework. First, the interface capturing  
 55 method is presented. It enables to follow the evolution of the interface between phases and to distribute in  
 56 space the respective physical properties by defining a mixing law. From this mixing law, a phase change  
 57 model will be derived and the Navier-Stokes equations will be consequently modified to take into account  
 58 the phase change model.

### 59 2.1. Level Set approach

60 In this section, we describe the level set method used to locate the interface between the liquid phase  
 61 and the vapor phase. It is a signed distance function and it is a widely used tool in different fields such as  
 62 crystal growth, image restoration or surface reconstruction [34]. Let  $\Omega$  be the whole domain,  $\Omega_l$  the liquid  
 63 domain and  $\Omega_v$  the vapor domain. The level set function is a signed distance function from the interface  
 64  $\Gamma = \Omega_l \cap \Omega_v$  defined at each node  $X$  of  $\Omega$  as follows:

$$\alpha(X) = \begin{cases} -\text{dist}(X, \Gamma) & \text{if } X \in \Omega_l, \\ 0 & \text{if } X \in \Gamma, \\ \text{dist}(X, \Gamma) & \text{if } X \in \Omega_v. \end{cases} \quad (1)$$

65 The evolution of the level set function is described by the following transport equation [35]

$$\frac{\partial \alpha}{\partial t} + u \cdot \nabla \alpha = 0, \quad (2)$$

66 where  $u$  is a velocity. The level set, as a distance function, verifies  $\|\nabla \alpha\| = 1$ . However, when the interface  
 67 is convected by  $u$ , the **level set** can lose this property, which may cause numerical instabilities, and needs  
 68 to be reinitialized to recover it. A common way to reinitialize it, is to solve the following Hamilton-Jacobi  
 69 equation [35]

$$\frac{\partial \alpha}{\partial \tau} + s(\alpha)(\|\nabla \alpha\| - 1) = 0, \quad (3)$$

70 where  $\tau$  is a pseudo-time and  $s(\alpha)$  is the sign function of  $\alpha$ . The steady state solution of this non-linear  
71 hyperbolic equation will be a distance function from the interface while keeping unchanged its zero isovalue.

72 Once the level set function is computed, we can distribute in space the corresponding physical properties  
73 (for example  $\rho_v$  and  $\rho_l$ , respectively vapor and liquid densities) using a mixing law as follows:

$$\rho = H(\alpha)\rho_v + (1 - H(\alpha))\rho_l, \quad (4)$$

74 where  $H$  is a smoothed Heaviside function used to obtain a better continuity at the interface and given by

$$H(\alpha) = \begin{cases} 1 & \text{if } \alpha > \varepsilon, \\ \frac{1}{2} \left( 1 + \frac{\alpha}{\varepsilon} + \frac{1}{\pi} \sin \left( \frac{\pi \alpha}{\varepsilon} \right) \right) & \text{if } |\alpha| \leq \varepsilon, \\ 0 & \text{if } \alpha < -\varepsilon. \end{cases} \quad (5)$$

75 Here  $\varepsilon$  is a small parameter such that  $\varepsilon = O(h_{\text{im}})$ , known as the interface thickness, and  $h_{\text{im}}$  is the mesh  
76 size in the normal direction to the interface. In the vicinity of the interface, it can be computed using

$$h_{\text{im}} = \max_{j,l \in K} \nabla \alpha \cdot \mathbf{x}^{jl}, \quad (6)$$

77 where  $K$  is the mesh element under consideration and  $\mathbf{x}^{jl} = \mathbf{x}^l - \mathbf{x}^j$  represents the edge connecting the  
78 nodes  $\mathbf{x}^j$  and  $\mathbf{x}^l$  of  $K$ .

## 79 2.2. Phase change model

80 In this section, we derive a pseudo-compressible model accounting for mass transfer at the interface.  
81 From the mass conservation equation, we will quantify the exchange of mass between the vapor and the  
82 liquid phases. To take into account this exchange of mass, the Navier-Stokes equations and the level set  
83 equation will be modified. Such derivation has already been done in the previous work of Denis [36], in the  
84 context of finite difference method.

### 85 2.2.1. Derivation of the governing equations for the phase change

86 We recall the Navier-Stokes equations:

$$87 \quad \rho(\partial_t u + u \cdot \nabla u) - \nabla \cdot (2\mu \varepsilon(u)) + \nabla p = f_{ST} + f, \quad (7)$$

$$88 \quad \frac{\partial \rho}{\partial t} + \nabla \cdot (\rho u) = 0, \quad (8)$$

89 where  $u$ ,  $p$ ,  $\rho$ ,  $\mu$ ,  $f_{ST}$  and  $f$  are the velocity, the pressure, the density, the viscosity, the surface tension force  
 90 and additional source term of the momentum equation respectively.

91 The derivation of the model relies on the mixing law used to distribute the density in space. Therefore,  
 92 we first define a mixing law for the density

$$\rho = (\rho_v - \rho_l)H(\alpha) + \rho_l, \quad (9)$$

93 where  $H$  is a Heaviside function. The mass conservation in the domain  $\Omega$  reads

$$\frac{\partial \rho}{\partial t} + \nabla \cdot (\rho u) = 0. \quad (10)$$

94 We define a surface mass transfer rate  $\dot{m}[kg.m^{-2}.s^{-1}]$  to quantify the exchange of mass between the liquid  
 95 and vapor phases:

$$\frac{\partial}{\partial t} (\rho_v H(\alpha)) + \nabla \cdot (\rho_v H(\alpha) u) = \dot{m} |\nabla \alpha| \delta(\alpha), \quad (11)$$

$$\frac{\partial}{\partial t} ((1 - H(\alpha)) \rho_l) + \nabla \cdot (\rho_l (1 - H(\alpha)) u) = -\dot{m} |\nabla \alpha| \delta(\alpha), \quad (12)$$

98 where  $\delta$  is a Dirac function. Expanding (11) and (12) leads to

$$\rho_v \frac{\partial H(\alpha)}{\partial t} + \rho_v H(\alpha) \nabla \cdot u + \rho_v u \cdot \nabla H(\alpha) = \dot{m} |\nabla \alpha| \delta(\alpha), \quad (13)$$

$$-\rho_l \frac{\partial H(\alpha)}{\partial t} + \rho_l (1 - H(\alpha)) \nabla \cdot u - \rho_l u \cdot \nabla H(\alpha) = -\dot{m} |\nabla \alpha| \delta(\alpha). \quad (14)$$

101 By dividing (13) and (14) by their respective density and summing, we obtain the new mass conservation  
 102 equation

$$\nabla \cdot u = \dot{m} \left( \frac{1}{\rho_v} - \frac{1}{\rho_l} \right) |\nabla \alpha| \delta(\alpha). \quad (15)$$

103 The velocity is not divergence free since a mass transfer occurs at the interface between the vapor and the  
 104 liquid.

105 Since a transfer of mass occurs, the level set equation will be modified to advect the level set not only  
 106 from the velocity obtained through the resolution of the Navier-Stokes equations but also the velocity of the  
 107 vapor front. This is obtained by summing (13) and (14) and dividing by  $(\rho_v - \rho_l)$ :

$$\frac{\partial H(\alpha)}{\partial t} + u \cdot \nabla H(\alpha) = \frac{\rho}{\rho_l - \rho_v} \nabla \cdot u. \quad (16)$$

108 Considering the derivative in time and in space of the Heaviside function,  $\frac{\partial H(\alpha)}{\partial t} = \frac{\partial H(\alpha)}{\partial \alpha} \frac{\partial \alpha}{\partial t} = \delta(\alpha) \frac{\partial \alpha}{\partial t}$  and  
 109  $\nabla H(\alpha) = \delta(\alpha) \nabla \alpha$ , we obtain

$$\delta(\alpha) \frac{\partial \alpha}{\partial t} + \delta(\alpha) u \cdot \nabla \alpha = \frac{\rho}{\rho_l - \rho_v} \nabla \cdot u. \quad (17)$$

110 In the case of a divergence free velocity fields, Eq (17) resumes to the standard level set equation. Replacing  
 111  $\nabla \cdot u$  by (15) leads to

$$\delta(\alpha) \frac{\partial \alpha}{\partial t} + \delta(\alpha) u \cdot \nabla \alpha = \frac{\rho}{\rho_l - \rho_v} \dot{m} \left( \frac{1}{\rho_v} - \frac{1}{\rho_l} \right) |\nabla \alpha| \delta(\alpha). \quad (18)$$

112 Extending to the whole domain and simplifying leads to

$$\frac{\partial \alpha}{\partial t} + u \cdot \nabla \alpha = \frac{\rho}{\rho_l \rho_v} \dot{m} |\nabla \alpha|. \quad (19)$$

113 The level set equation now reads

$$\frac{\partial \alpha}{\partial t} + \left[ u - \frac{\rho}{\rho_l \rho_v} \dot{m} \frac{\nabla \alpha}{|\nabla \alpha|} \right] \cdot \nabla \alpha = 0. \quad (20)$$

114 The level set is now advected by the velocity  $u$  obtained from the resolution of the Navier-Stokes and by  
 115 a velocity representing the vaporization of the water.

116 Similarly, one can use the same derivation for the energy equation. Neglecting the heat generated by  
 117 viscosity forces and capillary forces, the energy equation reads

$$\rho c_p \left( \frac{\partial T}{\partial t} + u \cdot \nabla T \right) - \nabla \cdot (k \nabla T) = - (L + (c_p^v - c_p^l)(T - T_{\text{sat}})) \dot{m} \delta(\alpha) |\nabla \alpha| \frac{\rho^2}{\rho_v \rho_l}. \quad (21)$$

118 where  $T$  is the temperature,  $T_{\text{sat}}$  is the saturation temperature,  $c_p$  is the specific heat,  $c_p^v$  (resp.  $c_p^l$ ) is the  
 119 specific heat in the vapor (resp. in the liquid) and  $k$  is the thermal conductivity. The formulation accounts  
 120 naturally for the thickness of the interface. It is a generic formulation that requires the definition of the  
 121 mass transfer rate  $\dot{m}$ .

122 *Remark 1.* The smoothing of the sharp mass flux presented in [37], using an averaged density is automatically  
 123 obtained in (19). The origin of the smoothing is due to the smoothing of the distribution of the density  
 124 across the interface.

### 125 2.2.2. Derivation of the surface mass transfer rate

126 The mass transfer rate is resolved using the heat released by an elementary volume  $dV$  of liquid that has  
 127 vaporized between the time  $t$  and  $t + dt$ . We consider a domain composed of water and vapor (see Figure 1).  
 128 The position of the interface at the time  $t$  is given by  $\alpha(t)$ ,  $dS$  and  $n$  being respectively the corresponding  
 129 elementary surface and its normal pointing in the vapor direction.

130 The heat released  $dQ$  by a volume  $dV$  of liquid that has vaporized during the elapsed time between  $t$   
 131 and  $t + dt$  is:

$$dQ = \rho_l L dV \quad (22)$$

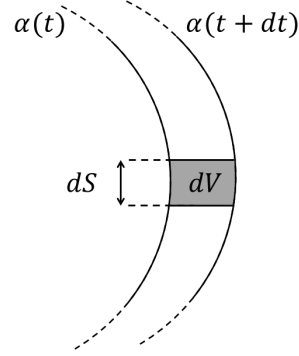


Figure 1: Volume  $dV$  that has vaporized between  $t$  and  $t + dt$ .

132 where  $L$  is the enthalpy of vaporization [ $J.kg^{-1}$ ]. The heat fluxes are defined respectively in the vapor and  
 133 the liquid by  $\phi_v = -k_v \nabla T_v$  and  $\phi_l = -k_l \nabla T_l$  where  $k_v$  and  $k_l$  are the thermal conductivity in the vapor  
 134 and the liquid respectively. Vaporization (resp. condensation) occurs when the jump of fluxes across the  
 135 interface  $[[\phi]] = [\phi_v - \phi_l]_{|\alpha=0} \cdot n$  is positive (resp. negative). Then  $dQ$  reads:

$$dQ = \int_{t'=t}^{t+dt} [[\phi]] dS dt'. \quad (23)$$

136 Differentiating and taking the limit for  $dt \rightarrow 0$  leads to

$$\lim_{dt \rightarrow 0} \rho_l L \frac{\alpha(t + dt) - \alpha(t)}{dt} = \lim_{dt \rightarrow 0} \frac{1}{dt} \int_{t'=t}^{t+dt} (-k_v \nabla T_v + k_l \nabla T_l)_{|\alpha=0} \cdot n dt'. \quad (24)$$

137 We obtain the surface mass transfer rate, the so-called Stefan condition,

$$\dot{m} = \rho_l L \frac{d\alpha}{dt} = (-k_v \nabla T_v + k_l \nabla T_l)_{|\alpha=0} \cdot n. \quad (25)$$

138 Eq. (25) requires the evaluation of the balance of fluxes at the interface  $(-k_v \nabla T_v + k_l \nabla T_l)_{|\alpha=0} \cdot n$ . This  
 139 evaluation is not straightforward when using an implicit definition of the interface. We therefore choose  
 140 to use a delta formulation. Approximating the surface integral by mean of a delta Dirac function on each  
 141 elementary volume  $\Omega_i$  containing the surface  $S_i$  leads to

$$\int_{S_i} (-k_v \nabla T_v + k_l \nabla T_l)_{|\alpha=0} \cdot n dS_i = \int_{\Omega_i} \delta(\alpha) (-k_v \nabla T_v + k_l \nabla T_l) \cdot n d\Omega_i. \quad (26)$$

142 Then, integrating (25) over  $\Omega_i$  gives an expression for the surface mass transfer  $\dot{m}$ :

$$\dot{m} = \frac{\int_{\Omega_i} \delta(\alpha) (-k_v \nabla T_v + k_l \nabla T_l) \cdot n d\Omega_i}{\int_{\Omega_i} \delta(\alpha) d\Omega_i}. \quad (27)$$

143 *2.3. Implicit surface tension*

144 A common way to introduce the surface tension in the Navier-Stokes equations is to use the Continuum  
 145 Surface Force model [38]. It consists first in rewriting the surface force as a volume one as follows:

$$f_{ST} = -\gamma\kappa\delta\mathbf{n}. \quad (28)$$

146 where  $\gamma$  is the surface tension coefficient,  $\delta$  is a Dirac function locating the interface,  $\kappa$  is the mean curvature  
 147 and  $n$  is the normal to the interface. Then (28) is used as a source term in the momentum equation (8).  
 148 However, an explicit implementation imposes the following severe restriction on the time step [38]:

$$\Delta t < (\Delta x)^{\frac{3}{2}} \sqrt{\frac{\rho_l + \rho_v}{4\pi\gamma}}. \quad (29)$$

149 If this time step restriction is not respected, spurious oscillations pollute the solution and destabilize the  
 150 interface. However, this time step restriction penalizes the computational cost of numerical simulations since  
 151 it is one or two orders of magnitude lower than the time step restriction of a CFL condition. To alleviate this  
 152 restriction, we use the approach developed in [39] and widely used in [25, 40, 41]. Using differential geometry,  
 153 the surface Laplacian  $\Delta_s I_\Gamma$  of an identity mapping function is  $-\kappa\mathbf{n}$ . We apply the surface Laplacian operator  
 154  $\Delta_S$  on  $I_\Gamma^{n+1} = I_\Gamma^n + \mathbf{u}^{n+1}\Delta t$  which represents the evolution in time of an interface. The surface Laplacian can  
 155 be decomposed into a standard Laplacian  $\nabla^2 u - \frac{\partial^2 u}{\partial \mathbf{n}^2} - \kappa \frac{\partial u}{\partial \mathbf{n}}$ . Multiplying by the surface tension coefficient  
 156 leads to the new expression for the surface tension:

$$f_{ST} = -\gamma\kappa\delta\mathbf{n} - \gamma\delta\Delta t \left( \frac{\partial^2 \mathbf{u}}{\partial \mathbf{n}^2} + \kappa \frac{\partial \mathbf{u}}{\partial \mathbf{n}} - \nabla^2 \mathbf{u}^{n+1} \right). \quad (30)$$

157 The usual term  $-\gamma\kappa\delta\mathbf{n}$  is now completed by additional terms proportional to the time step. These additional  
 158 terms act as an isotropic diffusion minus a diffusion in the normal direction of the interface. More details  
 159 are provided in [25].

160 *2.4. Variational MultiScale method for the Navier-Stokes equations*

161 Following the developments from previous sections, we generalize the Navier-Stokes equations, into:

162 *Find the velocity  $u$  and the pressure  $p$  such that:*

$$\rho(\partial_t u + u \cdot \nabla u) - \nabla \cdot (2\mu\varepsilon(u)) + \nabla p = f_{ST} + f, \quad (31)$$

$$\nabla \cdot u = f_c, \quad (32)$$

165 where  $\rho$ ,  $\mu$ ,  $f_{ST}$ ,  $f$  and  $f_c$  are the density, the viscosity, the surface tension force, additional source term of  
 166 the momentum equation and the source term of the continuity equation respectively.

167 The stability of the discrete formulation of Navier-Stokes depends on appropriate compatibility restric-  
 168 tions on the choice of the finite element spaces for the velocity and the pressure. Standard Galerkin mixed

169 elements with continuous equal order linear/linear interpolation is not a stable discretization and exhibits un-  
 170 controllable oscillations that pollute the solution. The Variational MultiScale method, proposed by Hughes  
 171 [42, 43], offers a general framework that deals with different and new variant of mixed variational formula-  
 172 tions [44–47]. We briefly recall here the main steps.

173 First, let us consider a decomposition of the velocity and the pressure fields into resolvable coarse-scale  
 174 and unresolved fine-scale:

$$175 \quad u = u_h + \tilde{u}, \quad (33)$$

$$176 \quad p = p_h + \tilde{p}, \quad (34)$$

177 Likewise, we apply the same decomposition for the weighting functions. The unresolved fine-scales are  
 178 usually modeled using residual based terms that are derived consistently. The static condensation consists  
 179 in substituting the fine-scale solution into the large-scale problem providing additional terms, tuned by  
 180 a local stabilizing parameter. The latter enhances the stability and accuracy of the standard Galerkin  
 181 formulation.

182 Second, to derive the stabilized formulation, we solve the fine scale problem, defined on the sum of  
 183 element interiors and written in terms of the time-dependent large-scale variables. Then we substitute in  
 184 the coarse problem, the fine-scale solution approximated within each element by:

$$185 \quad \tilde{u} = \sum_{\tau_h} \tau_u \tilde{P}_u(R_u), \quad (35)$$

$$186 \quad \tilde{p} = \sum_{\tau_c} \tau_c \tilde{P}_c(R_c), \quad (36)$$

187 where  $R_u$  and  $R_c$  are the finite element residuals.  $\tilde{P}_u$  and  $\tilde{P}_p$  are projection operators taken as the identity  
 188 in this work.  $\tau_u$  and  $\tau_c$  are the so called stabilization parameters. Thus, we eliminate the explicit appearance  
 189 of the fine-scale while still modeling their effects. More details are provided in [25, 29].

190 To simplify the notation, we use  $f_m$  and  $f_c$  as the source terms in (31)-(32), adding the explicit terms  
 191 of (30) into  $f_m$ . Inserting the expression for the subscales, we finally obtain the stabilized finite element  
 192 problem. The new variational formulation reads for the coarse scale,

$$\left\{ \begin{array}{l} (\rho \partial_t(u_h + \tilde{u}), v_h) + (\rho(u_h + \tilde{u}) \cdot \nabla(u_h + \tilde{u}), v_h) - (p_h + \tilde{p}, \nabla \cdot v_h) \\ + (2\mu \varepsilon(u_h) : \varepsilon(v_h)) + (\gamma \delta \Delta t \nabla(u_h + \tilde{u}) : \nabla v_h) = (f_m, v_h) \quad \forall v_h \in V_{h,0}, \\ (\nabla \cdot (u_h + \tilde{u}), q_h) = (f_c, q_h) \quad \forall q_h \in Q_h, \end{array} \right. \quad (37)$$

193 and for the fine scale,

$$\left\{ \begin{array}{l} (\rho \partial_t (u_h + \tilde{u}), \tilde{v}) + (\rho (u_h + \tilde{u}) \cdot \nabla (u_h + \tilde{u}), \tilde{v}) - (p_h + \tilde{p}, \nabla \cdot \tilde{v}) \\ + (2\mu \varepsilon(\tilde{u}) : \varepsilon(\tilde{v})) + (\gamma \delta \Delta t \nabla (u_h + \tilde{u}) : \nabla \tilde{v}) = (f_m, \tilde{v}) \quad \forall \tilde{v} \in \tilde{V}, \\ (\nabla \cdot (u_h + \tilde{u}), \tilde{q}) = (f_c, \tilde{q}) \quad \forall \tilde{q} \in \tilde{Q}. \end{array} \right. \quad (38)$$

194 At this level, two assumptions can be made to simplify the resolution of the fine scale equation: the subscales  
 195 are considered quasi-static and the convection is approximated by  $(u_h + \tilde{u}) \cdot \nabla (u_h + \tilde{u}) \approx u_h^c \cdot \nabla (u_h + \tilde{u})$ .  
 196 Therefore, by formulating the expression of  $\tilde{u}$  and  $\tilde{p}$  by substituting them into the large-scales equation, and  
 197 applying integration by parts, the system to solve becomes finally

$$\left\{ \begin{array}{l} (\rho \partial_t u_h, v_h) + (\rho u_h^c \cdot \nabla u_h, v_h) - (p_h, \nabla \cdot v_h) + (2\mu \varepsilon(u_h) : \varepsilon(v_h)) + (\gamma \delta \Delta t \nabla u_h : \nabla v_h) \\ - \sum_{K \in \mathcal{T}_h} (\tau_u R_u, \rho u_h^c \cdot \nabla v_h) - \sum_{K \in \mathcal{T}_h} (\tau_c R_c, \nabla \cdot v_h) = (f_m, v_h) \quad \forall v_h \in V_{h,0}, \\ (\nabla \cdot u_h, q_h) - \sum_{K \in \mathcal{T}_h} (\tau_u R_u, \nabla q_h) = (f_c, q_h) \quad \forall q_h \in Q_h, \end{array} \right. \quad (39)$$

198 where  $R_u$  and  $R_c$  are the residuals defined by

$$\begin{aligned} R_u &= f_m - \rho \partial_t u_h - \rho u_h^c \cdot \nabla u_h - \nabla p_h, \\ R_c &= f_c - \nabla \cdot u_h. \end{aligned} \quad (40)$$

199 Note that in the case of strongly anisotropic meshes with highly stretched elements, the definition of the  
 200 stabilization parameters is still an open problem and plays a critical role in the design of the stabilizing coef-  
 201 ficients. In [25] the authors propose a particular choice of the stabilizing parameters suitable for anisotropic  
 202 partitions that we adopt here.

203 By comparing the standard Galerkin method with the proposed stable formulation, additional integrals  
 204 that are evaluated element-wise are involved. These additional terms, obtained by replacing the approxi-  
 205 mated  $\tilde{u}$  and  $\tilde{p}$  into the large-scale equation, represent the effects of the sub-grid scales and above all take  
 206 into account the modified surface tension terms. They are introduced in a consistent way to the Galerkin for-  
 207 mulation and enable to overcome the instability of the standard formulation arising in convection dominated  
 208 flows and to deal with the pressure instabilities [48].

### 209 3. Edge-based mesh adaptation for multiphase flows

210 Anisotropic mesh adaptation on unstructured meshes plays an important role in the efficient numerical  
 211 simulation of multiphase flow problems since it helps keeping high accuracy while reducing the dedicated  
 212 CPU time to these simulations [49, 50]. As it is shown in [25] and more recently in [51], anisotropic mesh  
 213 adaptation outperforms adaptive octree. Small features are captured more easily using anisotropic mesh

214 than using octree. The use of anisotropic mesh adaptation enables to reduce the number of integration points  
 215 by one order of magnitude [51]. The idea is to concentrate elements in regions where the solution exhibits  
 216 a rapid variation of either the solution or its derivatives. In this case, it would be the large temperature  
 217 gradients, the large jumps at the interfaces as well as the change in direction for the velocity fields. The  
 218 objective is then to get the smallest error possible while controlling the number of mesh nodes. A vector or  
 219 a scalar monitor function is used in order to control the size, shape and orientation of the elements of the  
 220 mesh to be generated. This function is usually designed to give an estimate of some measure of the solution  
 221 error which is then equidistributed over each mesh cell. The mesh adaptation algorithm is built in order to  
 222 compute a mesh and a numerical solution. At each stage, we compute a numerical solution on the current  
 223 mesh and we evaluate an estimation of the interpolation error. We set up a minimization problem that aims  
 224 at minimizing the interpolation error in the  $L_1$ -norm, independently of the problem at hand [32]. To take  
 225 into account the solution development, we derive an optimal metric that minimizes its interpolation error.  
 226 Therefore, a new mesh is generated according to this metric field. The originality in the approach lies also  
 227 in its simplicity to compute the metric and the associated edge-based error estimator developed below.

### 228 3.1. Edge-based error estimation

229 Let  $u_h$  be a P1 finite element approximation obtained by applying the Lagrange interpolation operator  
 230 to a regular function  $u \in C^2(\Omega)$ . At each vertex  $i$  of the mesh, we have  $U_i = u(x^i) = u_h(x^i)$  (where  $x^i$  are  
 231 the coordinates of the vertex  $i$ ). Let  $\Gamma(i)$  be the "patch" associated to a vertex  $x_i$  of the mesh defined as  
 232 the set of nodes which share one edge with  $x_i$ , and let us denote by  $x_{ij}$  the edge connecting  $x_i$  to  $x_j$  as in  
 Figure 2.

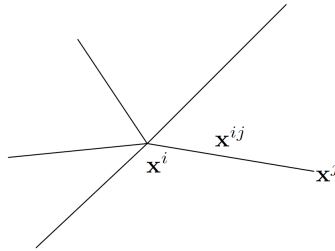


Figure 2: Patch associated with node  $x^i$

233

234 The gradient  $\nabla u^h \cdot x^{ij}$  on the edge  $x_{ij}$  is continuous, therefore we can write

$$235 \quad U^j = U^i + \nabla u^h \cdot x^{ij}, \quad (41)$$

236 which leads to

$$237 \quad \nabla u_h \cdot x^{ij} = U^j - U^i. \quad (42)$$

238 The work performed in [32] allows us to write the following error estimator:

$$239 \quad \|\nabla u^h \cdot x^{ij} - \nabla u(x^i) \cdot x^{ij}\| \leq \max_{y \in |x^i, x^j|} |x^{ij} \cdot H_u(y) \cdot x^{ij}|, \quad (43)$$

240 with  $H_u$  the Hessian of  $u$ . At the node  $x^i$ , we seek the recovered gradient  $g^i$  of  $u_h$

$$241 \quad \nabla g_h \cdot x^{ij} = g^j - g^i. \quad (44)$$

242 We want the projection of the Hessian based on the gradient at the extremities of the edge, thus we have

$$243 \quad (\nabla g_h \cdot x^{ij}) \cdot x^{ij} = (g^j - g^i) \cdot x^{ij}, \quad (45)$$

$$244 \quad (H_u \cdot x^{ij}) \cdot x^{ij} = g^{ij} \cdot x^{ij}, \quad (46)$$

245 with  $g^{ij} = g^j - g^i$ . It can be shown [32] that the quantity  $|g^{ij} \cdot x^{ij}|$  gives a second order accurate  
 246 approximation of the second derivative of  $u$  along the edge  $x^{ij}$ . Motivated by the fact that, for P1 finite  
 247 elements on anisotropic meshes, edge residuals dominate a posteriori errors, as proved in [52], it is therefore  
 248 suitable to define an error indicator function associated to the edge  $x^{ij}$  as

$$249 \quad e^{ij} = |g^{ij} \cdot x^{ij}|. \quad (47)$$

250 And this error, is the exact interpolation error along the edge and allows to evaluate the global  $L_1$  error.  
 251 However, the gradient is not know at the vertices, thus a recovery procedure has to be considered.

### 252 3.2. Gradient recovery procedure

253 The gradient recovery procedure relies on the following optimization problem:

$$254 \quad G^i = \arg \min_G \left( \sum_{j \in \Gamma(i)} |(G - \nabla u_h) \cdot x^{ij}|^2 \right), \quad (48)$$

255 where  $G^i$  is the recovered gradient. Denoting by  $\otimes$  the tensor product between two vectors, let us introduce  
 256  $X^i$  the length distribution tensor at node  $i$

$$257 \quad X^i = \frac{1}{|\Gamma(i)|} \left( \sum_{j \in \Gamma(i)} x^{ij} \otimes x^{ij} \right), \quad (49)$$

258 whose purpose is to give an average representation of the distribution of edges in the patch. Let us express  
 259 the recovered gradient  $G^i$  in terms of the length distribution tensor

$$260 \quad G^i = (X^i)^{-1} \sum_{j \in \Gamma(i)} U^{ij} x^{ij}. \quad (50)$$

261 Therefore, the estimated error  $e_{ij}$  is thus written as

$$262 \quad e_{ij} = G^{ij} \cdot x^{ij}. \quad (51)$$

263 *3.3. Metric construction*

264 In order to relate the error indicator defined in (51) to a metric suitable for a mesh adaptation procedure,  
 265 we introduce the concept of stretching factor  $s^{ij}$  defined as the ratio between the length of the edges  $x^{ij}$   
 266 after the adaptation procedure and after the adaptation procedure, [32]. The metric takes the following  
 267 expression:

$$268 \quad \widetilde{M}^i = (\widetilde{X}^i)^{-1}, \quad (52)$$

269 where  $\widetilde{X}^i$  is defined as:

$$270 \quad \widetilde{X}^i = \frac{1}{|\Gamma(i)|} \left( \sum_{j \in \Gamma(i)} s^{ij} \otimes s^{ij} \right). \quad (53)$$

271 The stretching factor  $s^{ij}$  of the edge  $ij$  is chosen so that the total number of nodes in the mesh is kept fixed  
 272 and is defined as

$$273 \quad s^{ij} = \left( \frac{e_{ij}}{e(N)} \right), \quad (54)$$

274 where  $e(N)$  is the total error .

275 *3.4. Mesh adaption criteria*

276 In multiphase applications, the material interface between liquid and gas need to be modeled accurately.  
 277 Two strategies are commonly used; we refer to them in this work as explicit and implicit adaptation. In  
 278 the first one, we design and pre-adapt the mesh around the boundaries and in some regions of interest. The  
 279 obtained adapted mesh will be used all along the simulation, provided that the flow exhibits a bounded level  
 280 of unsteadiness. The criteria for the mesh adaptation are geometric and do not depend on the solution.  
 281 Whereas, the implicit strategy imposes a dynamic mesh adaptation that changes the mesh frequently and  
 282 minimizes as possible the prescribed error. Consequently, it requires a criterion based solely on the solution.

283 The common way to adapt a mesh to several variables, such as the velocity and the level set function, is  
 284 to compute the metrics corresponding to each of them and then to produce a unique metric by an operation  
 285 known as the intersection of metrics. In this work, we simplify this operation and we use one metric that  
 286 account for different variables. Therefore, based on the theory proposed in the previous section, it is possible  
 287 to extend definition (47) to account for several sources of error. In the following numerical experiments,  
 288 the adaptivity accounts for the velocity components  $V_k$ , its magnitude  $|V|$ , the level set function  $\alpha$  and the  
 289 temperature  $T$ , by defining the following vector of sources of error:

$$\mathbf{v}(\mathbf{x}^i) = \left\{ \frac{V_k^i}{|V^i|}, \frac{|V^i|}{\max_j |V^j|}, \frac{\alpha^i}{\max(\alpha)}, \frac{T^i}{\max(T)} \right\}. \quad (55)$$

290 Because all fields are normalized (the velocity components  $V_x$ ,  $V_y$  and  $V_z$  by the local velocity norm,  
 291 the velocity norm  $|V|$ , the temperature and the level set function  $\alpha$  by their respective global maximum), a  
 292 field that is much larger in absolute value does not dominate the error estimator, and the variations of all  
 293 variables are fairly taken into account.

### 294 3.5. High-fidelity anisotropic meshing

295 We aim to show the flexibility of the proposed mesh adaptation technique to deal with multiphase flows.  
 296 Therefore we consider three fixed objects defined by level set functions inside a squared domain (see Figure 3).  
 297 The circle of radius 0.1m is centered at (0.15;0.15). The square of 0.20m size is centered at (0.85;0.15). The  
 298 regular pentagram is centered at (0.5;0.75) and the radius of the circumcircle is 0.2m. We choose to position  
 299 them close to the wall to assess the capacity of the method to capture the features of the geometry close to  
 300 a boundary.

301 In multiphase simulations, we use the level set function to define the properties in each phase. The  
 302 physical properties are usually discontinuous across the interface. To avoid discontinuities which lead to  
 303 numerical errors, we use a smooth Heaviside function computed from the level set function. This creates  
 304 an interface transition with a thickness of few elements. The use of mesh adaptation techniques enables to  
 305 reduce this thickness. As it is depicted in Figure 3, for a given number of elements (10,000), the transition  
 is finer with an anisotropic adaptive mesh.

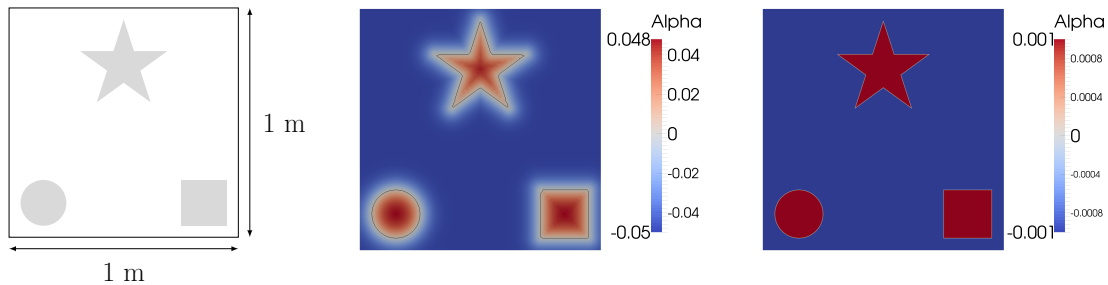


Figure 3: Three immersed objects inside a squared cavity (left). Filtered level set function for 10,000 elements in a structured mesh (middle) and in an adaptive mesh (right). The use of an adaptive mesh enables a finer interface transition. Respective meshes are shown in Figure 5.

306  
 307 Figure 4 shows the obtained zero isovalue of the level set functions using different number of nodes. The  
 308 comparison with structured meshes using the same number of nodes shows that anisotropic mesh adaptation  
 309 allows easily to keep very good accuracy of the geometry, even for a low number of nodes. Figure 5 shows  
 310 the correct orientation and deformation of the mesh elements (longest edges parallel to the boundary).  
 311 This yields a great reduction of the number of triangles. These results give confidence that the proposed  
 312 framework allows to deal with different shapes, with angles, singular point and curvatures.

313 Finally, in Figure 6, we measure the accuracy of the mesh adaptation technique. We compute the total  
 314 perimeter and the total area of the three immersed objects and we plot the error between the analytical  
 315 and the numerical solutions. We also plot the error for a structured mesh. Figure 6 confirms the advantage  
 316 of using anisotropic adaptive meshes for multiphase flows. For a given accuracy, at least ten times more  
 elements are required in a structured mesh.

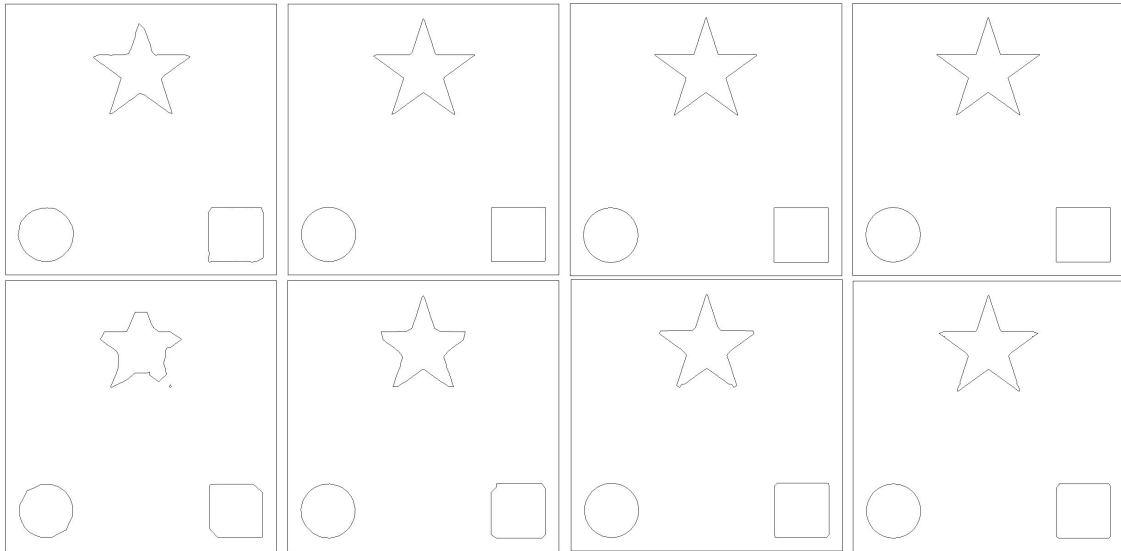


Figure 4: Zero isovalue of the level set function for 1,000, 2,000, 5,000 and 10,000 elements. First line: result with adaptive meshing. Second line: result with structured meshes.

317

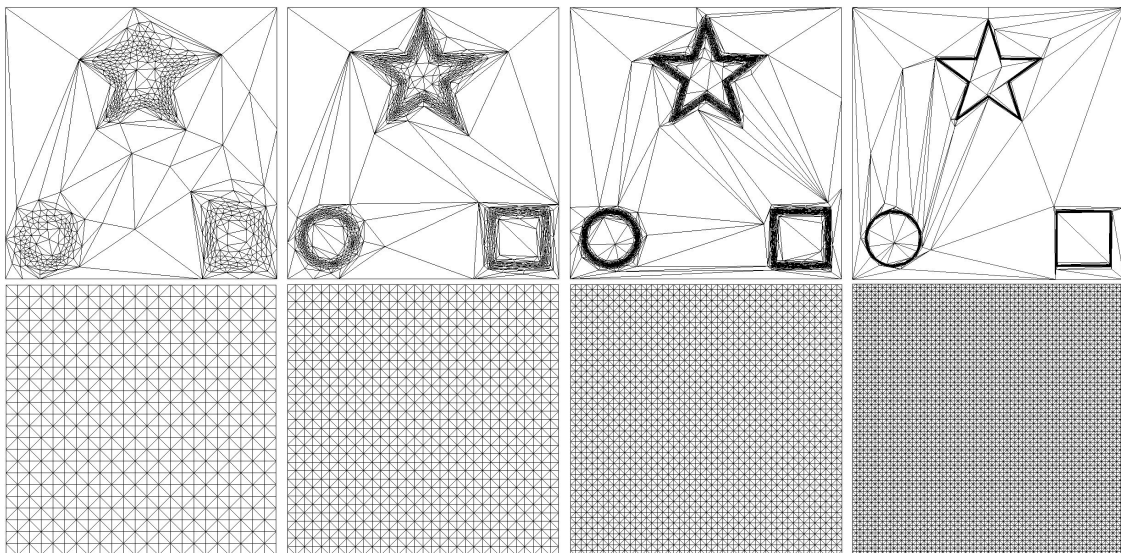


Figure 5: The obtained mesh for 1,000, 2,000, 5,000 and 10,000 elements.

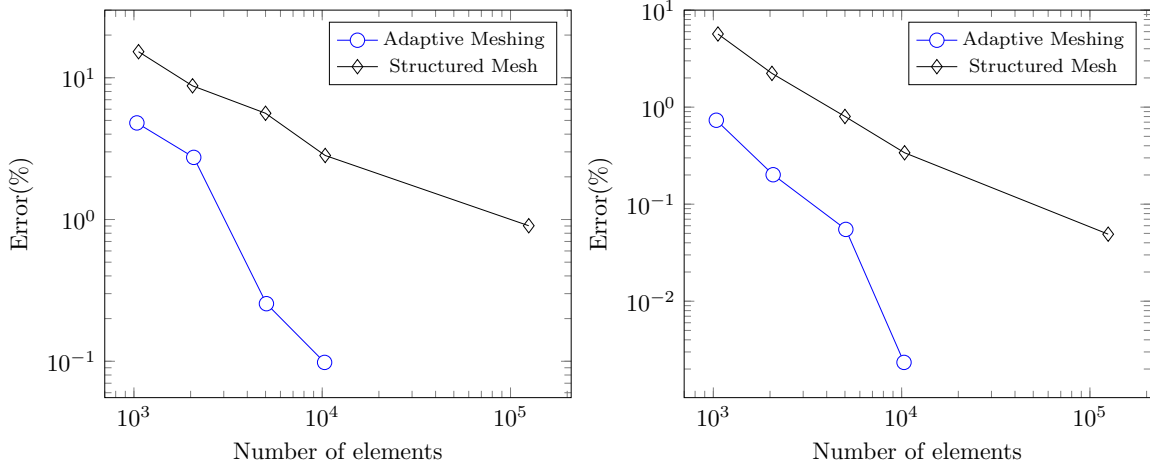


Figure 6: Percentage of error for the computation of the perimeter (left) and the area (right).

#### 318 4. Numerical examples

319 The proposed adaptive Eulerian framework for the simulation of both boiling and evaporation phenomena  
 320 is verified and validated in this section through a variety of test problems. Throughout this section, all the  
 321 obtained results will be compared to either analytical or numerical available solutions. In the last test case,  
 322 we bring forward a new problem with the experimental data on the cooling of a 3D heated solid inside a  
 323 water tank.

##### 324 4.1. Stefan problem

325 First, we consider the one-dimensional Stefan benchmark. It is a well known problem and serves as a  
 326 benchmark to assess the accuracy of phase change models [8, 11, 53]. It is defined schematically in Figure 7.  
 327 The domain is initially filled with water. The wall temperature is set constant and larger than the saturation  
 328 temperature. The water is at saturation temperature. At  $t > 0$ , a phase change occurs and induces a motion  
 329 of the interface between the vapor and the water. The convective term in the energy conservation equation  
 330 is neglected in both phases.

331 The position of the interface is given by

$$s(t) = 2\chi\sqrt{\alpha_v t}, \quad (56)$$

332 where  $\alpha_v$  is the thermal diffusivity defined by  $\alpha = k_v/(\rho_v c_p^v)$  and  $\chi$  is the solution of the transcendental  
 333 equation

$$\frac{T_{\text{sat}} - T_{\text{wall}}}{\sqrt{\pi}L} c_p^v = \chi \operatorname{erf}(\chi) \exp(\chi^2), \quad (57)$$

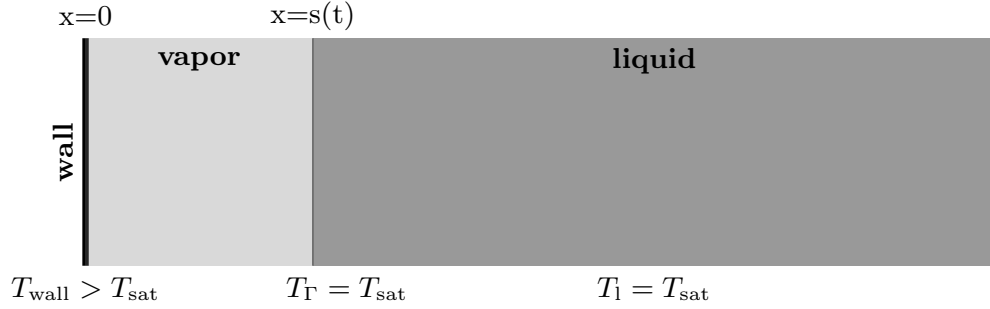


Figure 7: Initial setup for the classic Stefan problem.

334 derived in the case of a constant temperature in the liquid. The temperature in the vapor at a given time  $t$   
 335 is given by

$$T(x, t) = T_{\text{wall}} + \frac{T_{\text{sat}} - T_{\text{wall}}}{\text{erf}(\chi)} \text{erf}\left(\frac{x}{2\sqrt{\alpha_v t}}\right), \quad (58)$$

336 We consider the physical properties for the water and the vapor given in Table 1 and we consider  $T_{\text{wall}} - T_{\text{sat}} =$   
 337  $10\text{K}$ . We solve the transcendental equation using a Newton algorithm to find the value of  $\chi$ .

Table 1: Density, dynamic viscosity, specific heat and thermal conductivity for the vapor and the water at atmospheric pressure

	$\rho$ [kg/m <sup>3</sup> ]	$\mu$ [Pa·s]	$c_p$ [J/(kg·K)]	$k$ [W/(m·K)]	$L_{\text{sat}}$ [J/kg]
Vapor	0.597	$1.26 \times 10^{-5}$	2030	0.025	
Water	958.4	$2.8 \times 10^{-4}$	4216	0.679	$2.26 \times 10^6$

337  
 338 Figure 8 shows the evolution of the position of the interface for both the analytical and the numerical  
 339 solution having good agreement. Figure 9 shows that the use of a delta Dirac function to compute the mass  
 340 transfer rate results in a better convergence. This comparison was done by prescribing a maximum number  
 341 of iterations (3000) to reach a residual ( $10^{-7}$ ) using the GMRES method for the resolution of the linear  
 342 system.

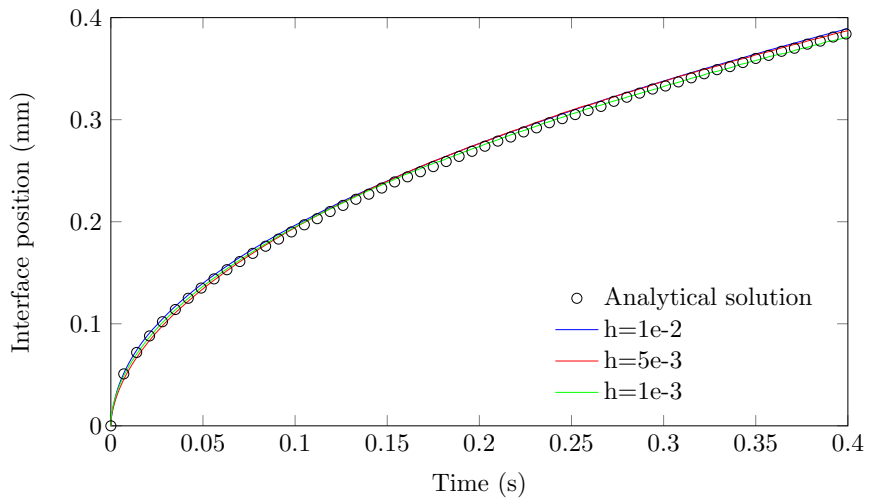


Figure 8: Evolution of the interface position for the Stefan problem.

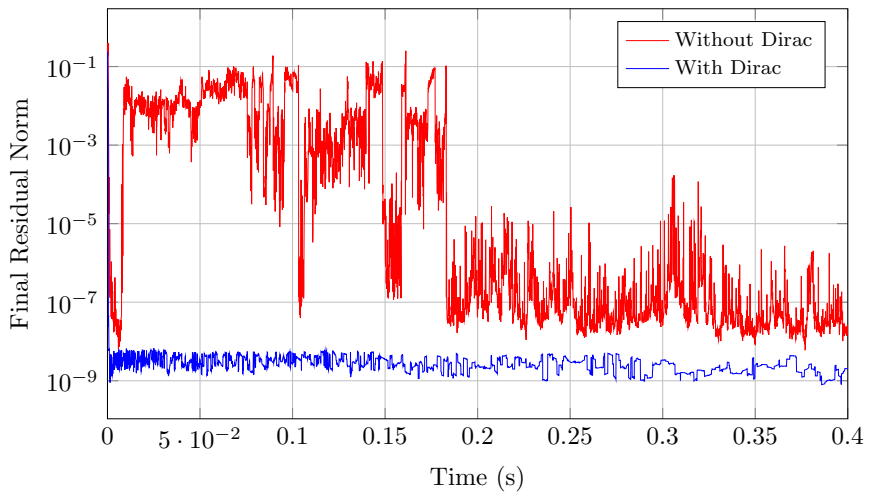


Figure 9: Final residual norm for the level set solver.

343 *4.2. 2D Film boiling*

344 This test case serves as a validation for the phase change model in several articles [1, 8, 14, 54]. Indeed,  
 345 when the temperature at the wall is much larger than the saturation temperature, a persistent layer of  
 346 vapor forms and remains between the wall and the water. This regime is known as film boiling. In the  
 347 configuration depicted in Figure 10, a Rayleigh-Taylor instability is triggered due to the low density fluid  
 348 below the high density fluid. Furthermore, the phase change will induce a growth of the film, amplifying  
 349 the instability.

For a Rayleigh Taylor instability, the most unstable Taylor wavelength is, in 2D,

$$\lambda_0 = 2\pi \left( \frac{3\gamma}{(\rho_l - \rho_g)g} \right)^{1/2}, \quad (59)$$

350 where  $\gamma$  is the surface tension.

351 The physical parameters taken from [8] are given in Table 2. For this set of parameters, the most unstable  
 352 wavelength is about  $\lambda_0 \approx 0.078\text{m}$ . Figure 10 shows the initial profile of the interface, defined by the following  
 353 function:

$$y = 0.5 + 0.4 \cos(2\pi x / \lambda_0). \quad (60)$$

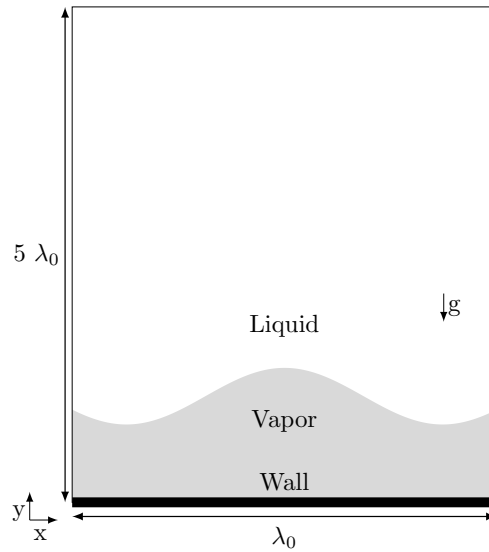


Figure 10: Setup for the 2D film boiling

354 Two cases will be studied. For the first case, the temperature at the wall is maintained constant at a  
 355 temperature of 5K above the saturation temperature and for the second, 10K. To assess the accuracy of the  
 356 computations, the authors in [1, 8, 54] used space-averaged Nusselt number obtained from the numerical

357 simulation and compare it to correlation found in the literature. The local Nusselt number defined as the  
 358 dimensionless heat flux through the wall is

$$Nu_u = \frac{\lambda_0}{T_w - T_{\text{sat}}} \left. \frac{\partial T}{\partial y} \right|_{y=0}. \quad (61)$$

359 Regarding the correlation of the Nusselt number in the literature, we use the correlation of Berenson [55]  
 360 and Klimenko [56] given by

$$Nu_B = 0.425(GrPr/Ja)^{1/4}, \quad (62)$$

361 and

$$Nu_K = 0.1691(GrPr/Ja)^{1/3} \text{ for } Ja < 0.71. \quad (63)$$

362 where the Grashof number  $Gr = \rho_v(\rho_l - \rho_v)g\lambda_0/\mu_v^2$  represents the ratio of the buoyancy force over the  
 363 viscous force, the Prandtl number  $Pr = \mu_v c_p^v/k_v$  represents the ratio of the momentum diffusivity over the  
 364 thermal diffusivity and the Jakob number  $Ja = c_p^v(T_w - T_{\text{sat}})$  the ratio of sensible heat over latent heat.

Table 2: Density, dynamic viscosity, specific heat and thermal conductivity for the vapor and the water at atmospheric pressure

	$\rho$ [kg/m <sup>3</sup> ]	$\mu$ [Pa·s]	$c_p$ [J/(kg·K)]	$k$ [W/(m·K)]	$L_{\text{sat}}$ [J/kg]
Vapor	5.0	0.005	200	1.0	
Water	200	0.1	400	40	$10^4$

365 Figure 11 shows the evolution of the temperature field and the interface for  $\Delta T = 10K$ . The vapor film  
 366 grows to a mushroom shape due to the Rayleigh-Taylor instability. Since we performed 2D computations,  
 367 no break up occurs due to surface tension. Therefore the mushroom cap rises along the channel followed  
 368 by a long and thin filament. Notice that due to the width of the channel, there is clearly an effect of the  
 369 lateral confinement on the shape of the vapor mushroom. Figure 12 shows the evolution of the mesh. The  
 370 mesh is adapted using the anisotropic mesh adaptation procedure presented in this paper, using only 25,000  
 371 elements. Therefore the mesh is very fine at the vapor/water interface and at the bottom when the thermal  
 372 gradient is the largest. The mesh remains coarse far from the interface, where the thermal gradient is null  
 373 and the velocity field is still 0.

374 The evolution of the space-averaged Nusselt number is depicted in Figure 13. The comparison with the  
 375 correlation of Berenson and Klimenko shows a good agreement for both cases.

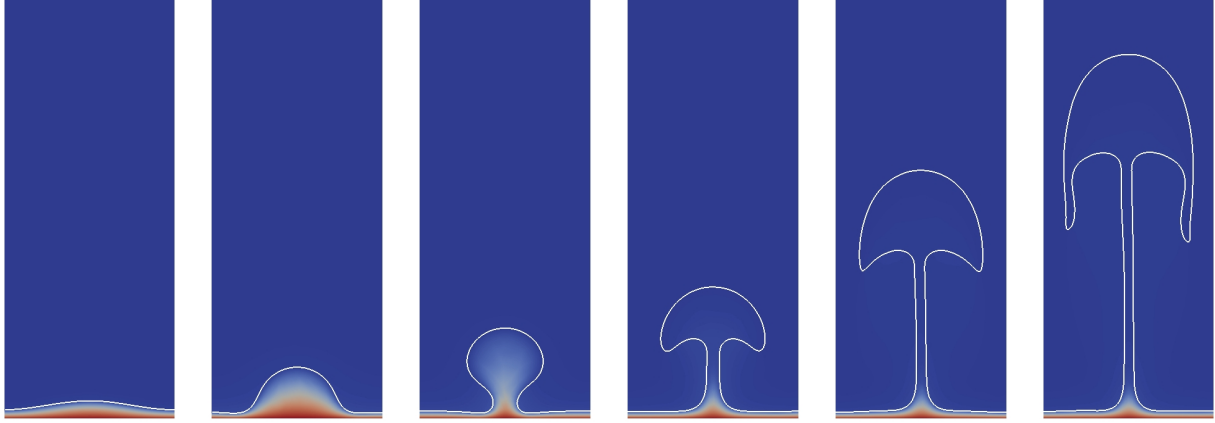


Figure 11: 2D Film boiling for  $\Delta T = 10K$ . Temperature field and interface location at  $t=0.01, 0.2, 0.3, 0.4, 0.7$  and  $1.0s$ . The interface is represented by the white line.

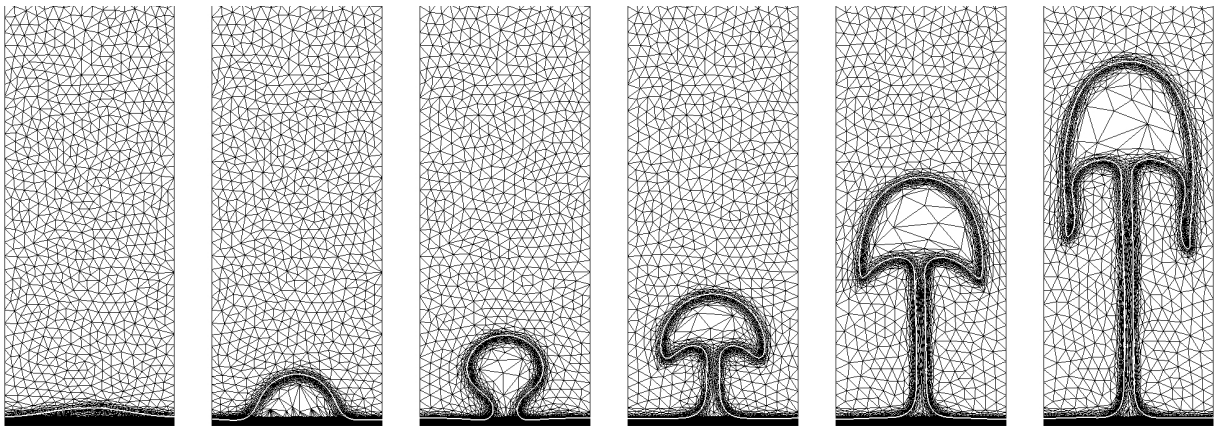


Figure 12: 2D Film boiling for  $\Delta T = 10K$ . Evolution of the mesh and the interface location at  $t=0.01, 0.2, 0.3, 0.4, 0.7$  and  $1.0s$ . The interface is represented by the white line.

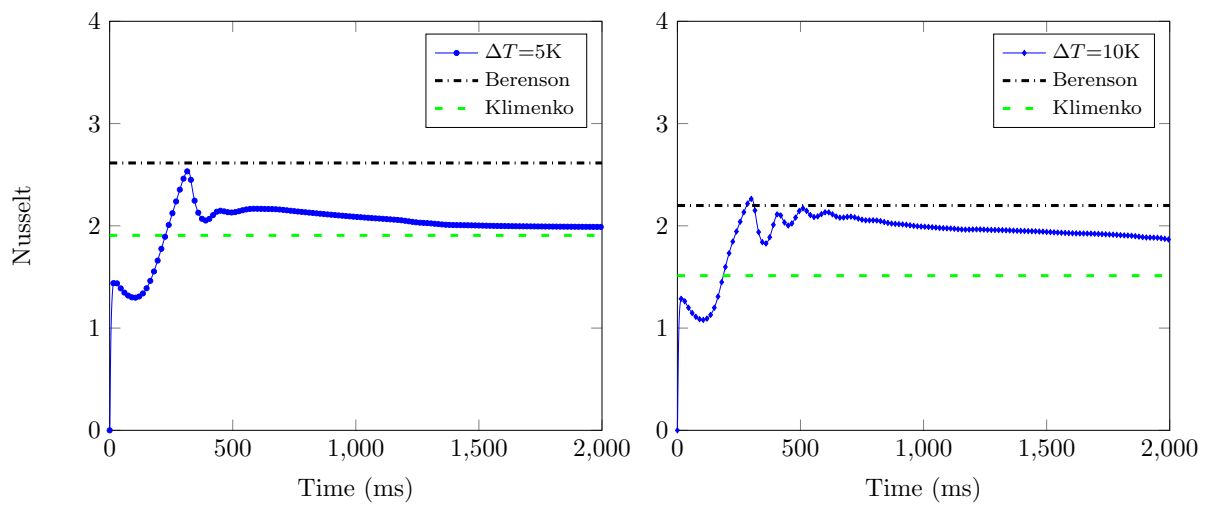


Figure 13: Evolution of the space-averaged Nusselt number for  $\Delta T = 5K$  (left) and  $\Delta T = 10K$  (right).

376 4.3. 3D boiling - sensitivity analysis

377 Several studies show that quench severity is dependent on different parameters: orientation, position,  
378 shape and size, agitation rate, fluid viscosity, and other variables. In this section, we will analyze at least  
379 the first three parameters. The objective is to show that the physical phenomena taking place are rich and  
380 that the experimental investigation remains generally limited. Indeed, the latter suffers from systematic  
381 revalidation of heat transfer coefficients when dealing with each parameter.

382 We consider then a water tank of dimension  $L \times L \times L$  (see Figure 14), filled to three quarters. Two  
383 geometries are proposed; a hot metallic cylinder of length 0.5m and diameter 0.1m with  $L=1$ m and a hot  
384 hollow cylinder (see Figure 18) of inner radius 3cm and outer radius of 6cm with  $L=0.40$ m.

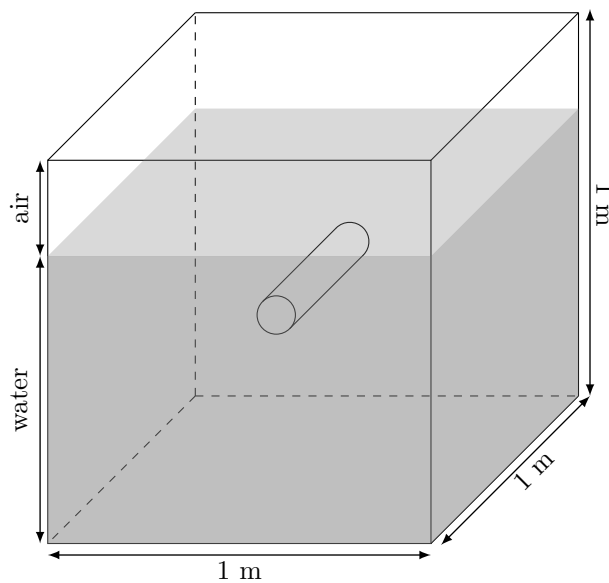


Figure 14: Set-up for the 3D film boiling

385 For the first geometry, three different configurations are considered. The cylinder is immersed horizontally  
386 at mid-height (see Figure 15), at a quarter of the height of the tank (see Figure 16) or vertically (see Figure  
387 17).

388 Figure 11 shows a persistent vapor film surrounds the cylinder. As expected, the position of the cylinder  
389 has an important effect on the film evolution and thus on the cooling velocity of the cylinder. Furthermore,  
390 such distance from the cylinder to the free surface has a direct impact on the overall flow inside the quenching  
391 bath. The higher the distance, the higher the velocity of the vapor phase breaking up at the surface.

392 Whereas, when the cylinder is immersed vertically inside the water tank, the shape of the film is totally  
393 different. Indeed, we can notice in Figure 12 a periodic release of the film all along the surface. Thus, the  
394 distribution of the flow is more concentrated at the top of the **cylinder**. This induces lower cooling velocity  
395 when compared to the previous case.

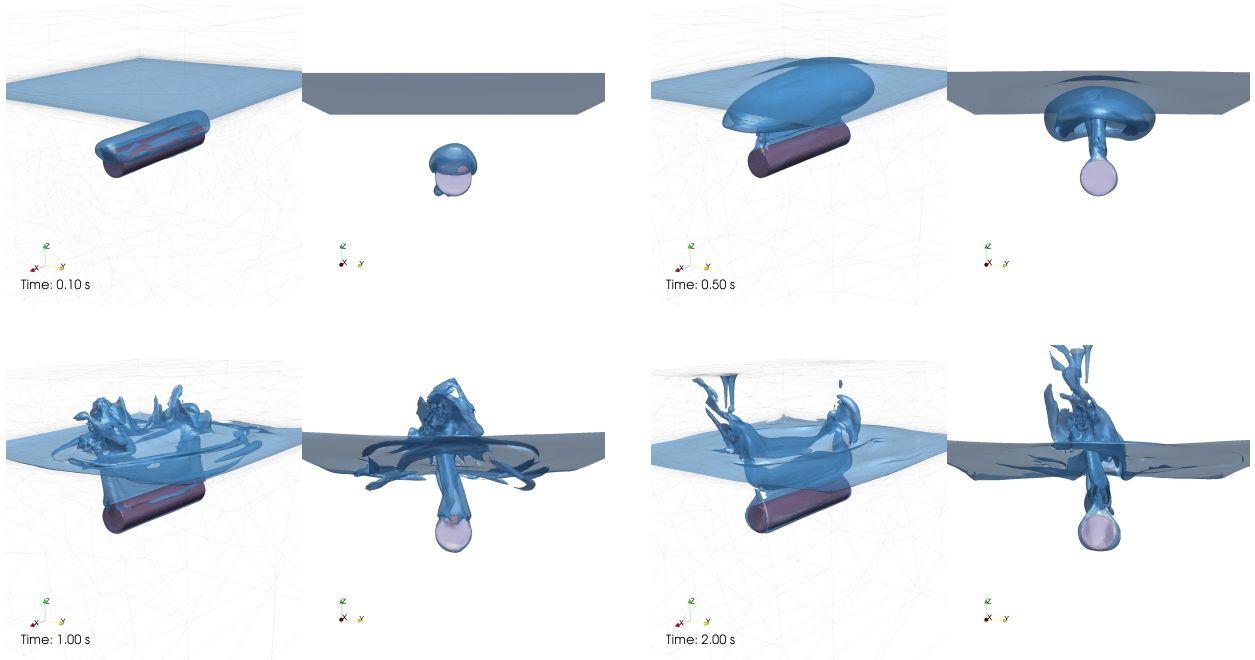


Figure 15: Cylinder at mid-height. Results at  $t=0.1, 0.5, 1$  and  $2$  s. Perspective view (left), front view (right).

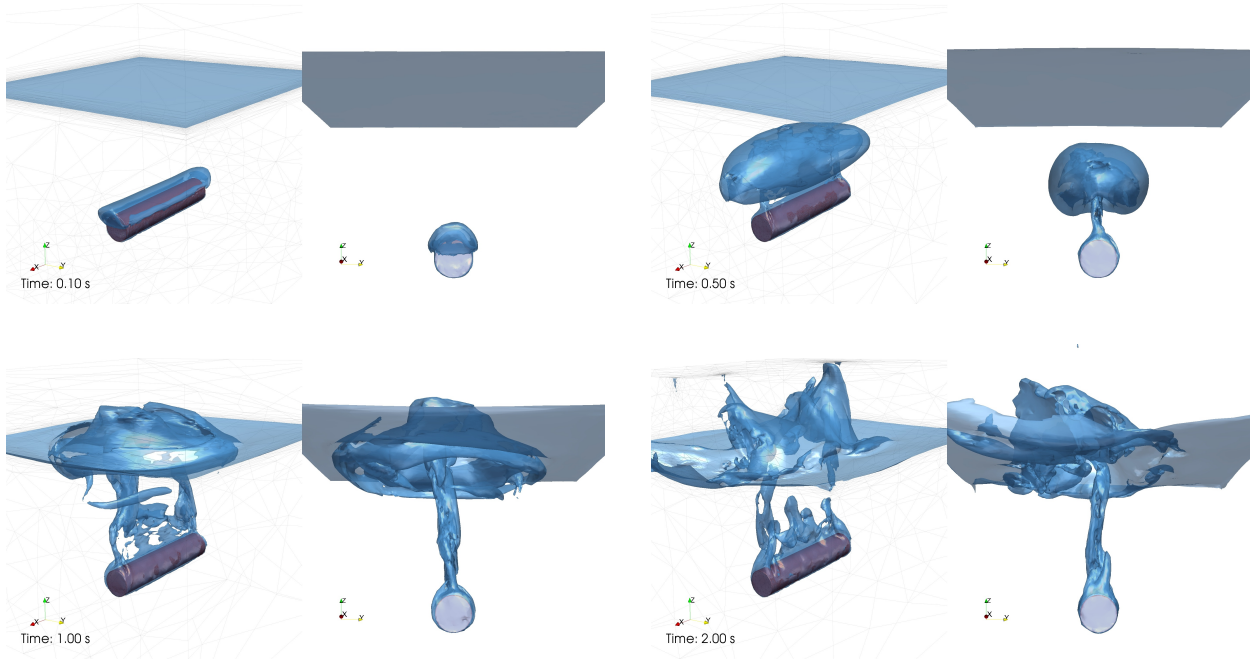


Figure 16: Cylinder at a quarter of the height. Results at  $t=0.1, 0.5, 1$  and  $2$  s. Perspective view (left), front view (right).

396 Finally, Figure 19 shows this time that both the size of the **hollow** cylinder and its geometrical features  
 397 seem to affect completely the flow. The boiling is well guided by the top surface with additional concentration

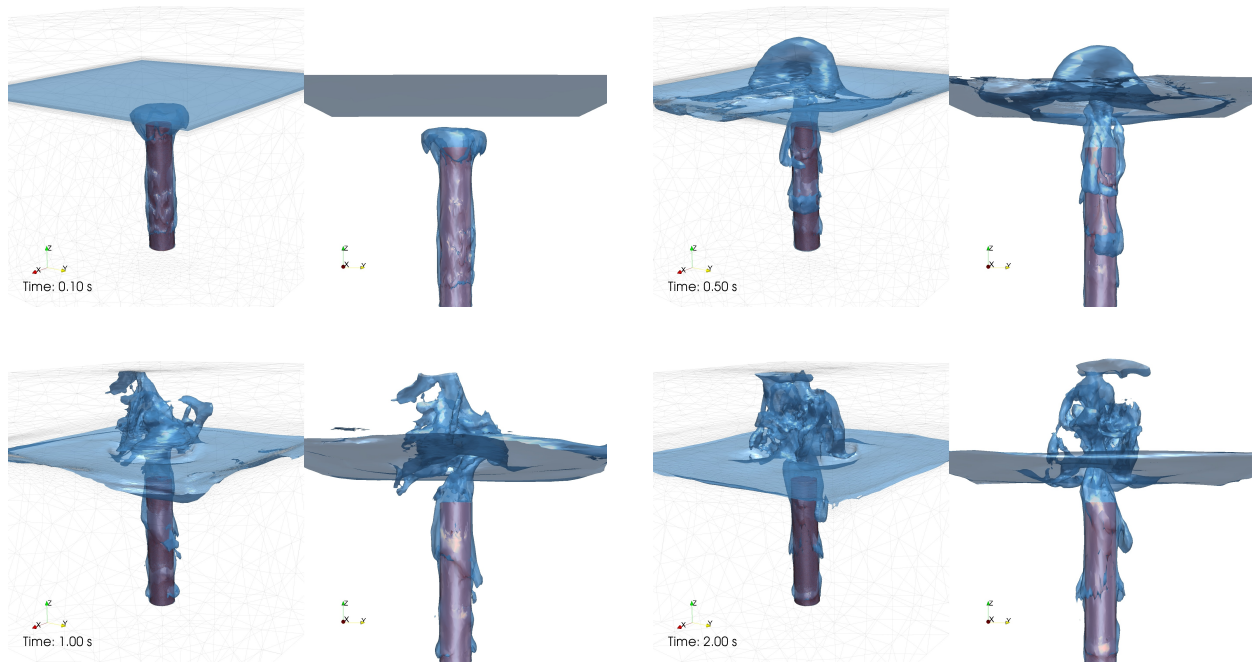


Figure 17: Vertical cylinder. Results at  $t=0.1, 0.5, 1$  and  $2$  s. Perspective view (left), front view (right).

398 along the extremity. This again confirms the important role of this adaptive Eulerian framework to predict  
 399 several liquid-vapor phase changes during boiling as well as to handle easily optimal combination of quench  
 400 parameters.

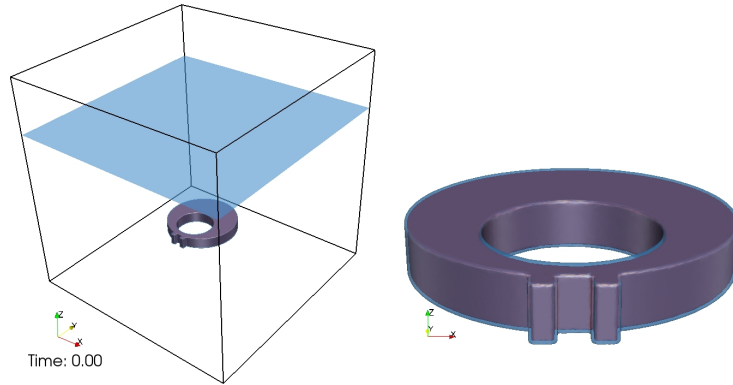


Figure 18: Hollow cylinder : Full domain with the ring (in red) and the gas-liquid interface in blue(left). Zoom on the ring (right)

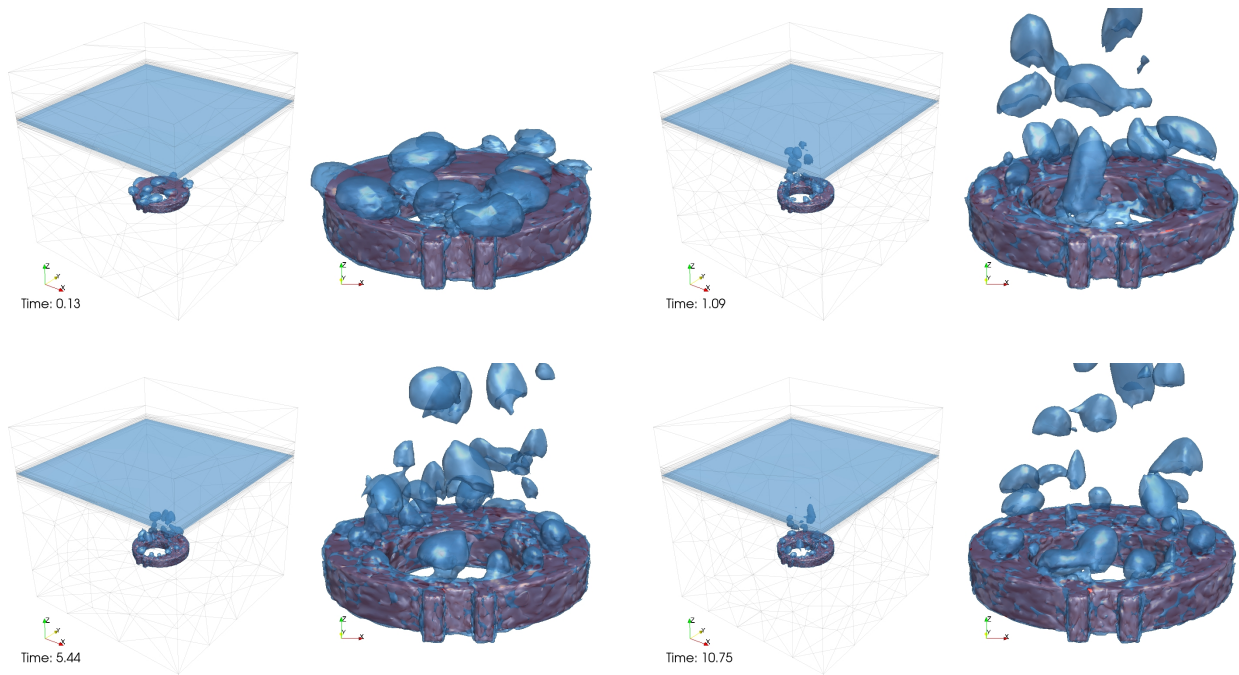


Figure 19: Hollow cylinder. Results at  $t=0.13, 1.09, 5.44$  and  $10.75$  s. Perspective view (left), front view (right).

401 4.4. Quenching of a solid, comparison with experimental data

402 We consider a domain of size  $0.60 \times 0.60 \times 0.40 \text{ m}^3$ , three-quarters full of water, in which a metallic  
 403 sample of dimension  $0.075 \times 0.075 \times 0.0015 \text{ m}^3$  is immersed (see Figure 20). The temperature of the sample  
 404 is  $T_{\text{solid}} = 880^\circ\text{C}$  and the temperature of the water is  $T_{\text{water}} = 25^\circ\text{C}$ . A thermocouple is placed at the core of  
 405 the metallic sample. From a practical point of view, due to the small thickness of the part, the temperature  
 406 at the core reflects the behavior of the temperature field at the interface.

407 A free slip boundary condition is prescribed on all the walls. The motion of the vapor film is due to the  
 408 buoyancy force and the surface tension force. The simulations are performed using the proposed adaptive  
 409 meshing technique with 200,000 tetrahedra. The time step is set to  $\Delta t = 0.002\text{s}$ .

410 All the physical parameters related to each phase are presented in Table 3.

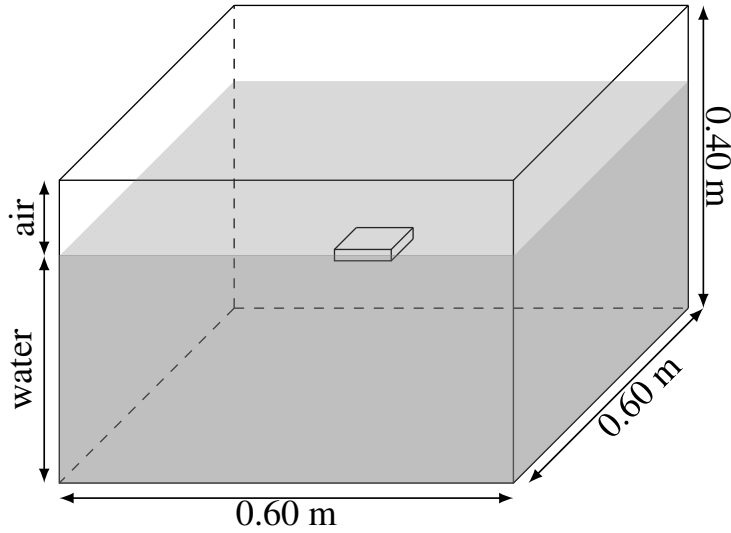


Figure 20: Set-up for the 3D industrial quenching

Table 3: Physical parameters defining the test case for the 3D industrial quenching

	$\rho$ [kg/m <sup>3</sup> ]	$\mu$ [Pa·s]	$c_p$ [J/(kg·K)]	$k$ [W/(m·K)]	$L_{\text{sat}}$ [J/kg]
Vapor	1.0	$1.2 \times 10^{-5}$	2010	0.025	$2.26 \times 10^6$
Water	1000	$1.0 \times 10^{-3}$	4185	0.6	
Solid	8000		435	11.4	

411 The evolution of the liquid-vapor phase is depicted in Figure 21 and shows again the ability of the  
 412 proposed Eulerian framework with adaptive meshing to deal with such challenging test case.

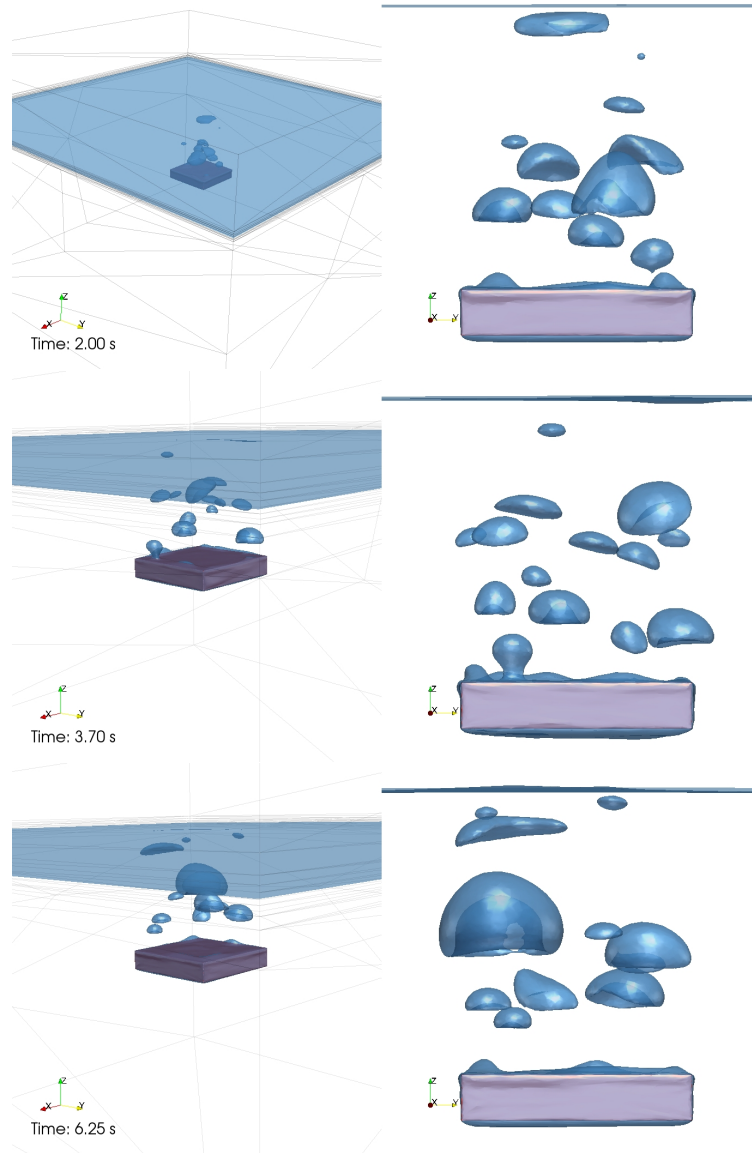


Figure 21: Industrial quenching. Results at  $t=2, 3.70$  et  $6.25$  s. Perspective view (left), front view (right). The zero isovalue of the level set is represented in blue.

413 Figure 22 represents a clip of the quenching tank. Water is depicted in blue and the solid in red. A slice  
 414 enables to visualize the adaptive mesh over time. At the top left corner, the picture shows the initial mesh,  
 415 mostly concentrated around the part and the free surface. As the simulation starts and bubbles form, the  
 416 mesh is adapted automatically at the level set interface. Under the constraint of a fixed number of elements,  
 417 one can notice that the mesh is coarsened automatically at the bottom of the tank, where the variation of  
 418 the solutions is small.

419 Finally, Figure 23 shows a good agreement for the temperature evolution between the experimental data

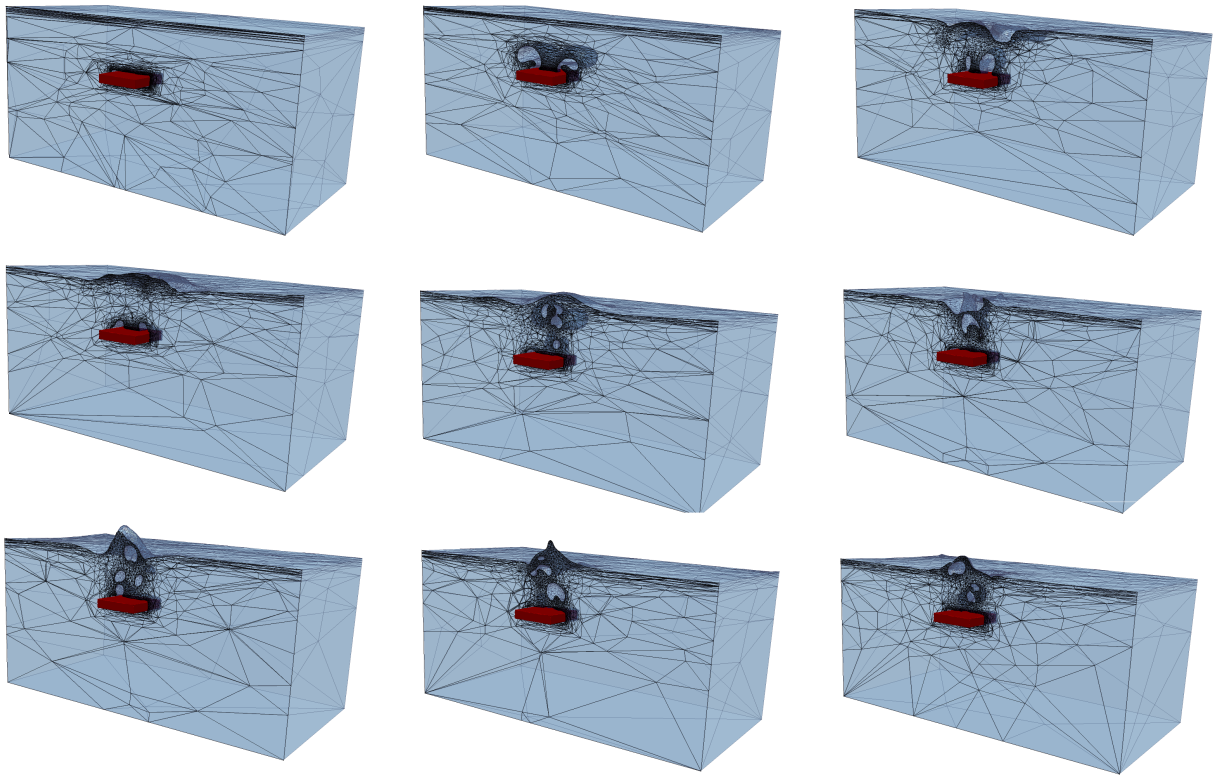


Figure 22: Industrial quenching: results at different instants. The solid is represented in red. A clip of the quenching tank, with visible adapted mesh.

420 and the numerical simulation. The strong coupling between the solid, the water and the vapor enables to  
421 perform such simulation without the use of a heat transfer coefficient at the solid boundaries. The anisotropic  
422 mesh adaptation enables to capture the large thermal gradient, the large jump at the interfaces as well as  
423 the complexity of the flow. Simulations are performed using 100,000 to 400,000 elements.

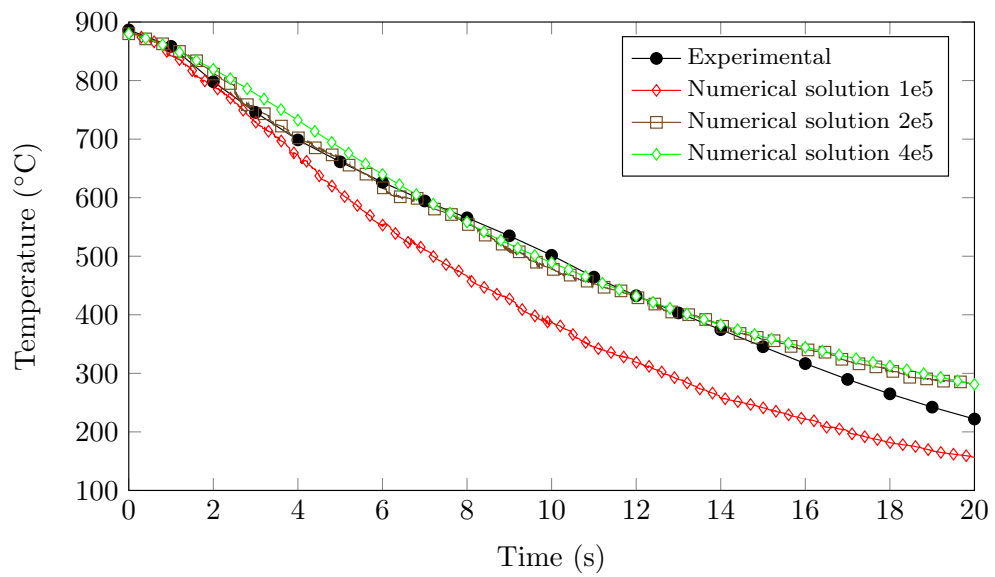


Figure 23: Evolution of the computed temperature at the core of the sample, sensitivity to the number of elements, comparison to experiments.

## 424 5. Conclusion

425 We proposed an adaptive Eulerian framework for the numerical simulation of the phase change and the  
426 evaporation that occurs at the interface between a heated solid surrounded by cooled liquid. We showed  
427 that in order to model efficiently these phenomena, the gas-liquid phase changes, the vapor formation and  
428 their dynamics, and the conjugate heat transfer must be solved simultaneously. Therefore, it replaces the  
429 use of classical assumptions and ad-hoc transfer coefficients. We have demonstrated the efficiency of this  
430 framework by performing challenging cases in 2D and 3D with comparisons including experimental data.  
431 For the first time, the direct numerical simulation of the solid-liquid-gas interaction for industrial quenching  
432 can be performed accurately.

## 433 Acknowledgments

434 The author gratefully acknowledges support from the companies involved in the ThosT project managed  
435 by Science Computer and Consultants (SCC): Areva NP, Aubert & Duval, Faurecia, Industeel CRMC  
436 (Arcelor Mittal), Lisi Aerospace and Snecma/Safran.

## 437 References

- 438 [1] A. Esmaeeli, G. Tryggvason, Computations of film boiling. Part I: numerical method , International Journal of Heat and  
439 Mass Transfer 47 (25) (2004) 5451 – 5461.
- 440 [2] A. Esmaeeli, G. Tryggvason, Computations of film boiling. Part II: multi-mode film boiling , International Journal of Heat  
441 and Mass Transfer 47 (25) (2004) 5463 – 5476.
- 442 [3] D. Juric, G. Tryggvason, Computations of boiling flows, International Journal of Multiphase Flow 24 (3) (1998) 387 – 410.
- 443 [4] G. Tryggvason, A. Esmaeeli, N. Al-Rawahi, Direct numerical simulations of flows with phase change, Computers &  
444 Structures 83 (67) (2005) 445 – 453.
- 445 [5] M. Irfan, M. Muradoglu, A front tracking method for direct numerical simulation of evaporation process in a multiphase  
446 system, Journal of Computational Physics 337 (2017) 132 – 153.
- 447 [6] F. Gibou, R. Fedkiw, S. Osher, A review of level-set methods and some recent applications, Journal of Computational  
448 Physics 353 (2018) 82 – 109.
- 449 [7] J. Papac, A. Helgadottir, C. Ratsch, F. Gibou, A level set approach for diffusion and Stefan-type problems with Robin  
450 boundary conditions on quadtree/octree adaptive Cartesian grids, Journal of Computational Physics 233 (2013) 241 –  
451 261.
- 452 [8] S. W. Welch, J. Wilson, A Volume of Fluid Based Method for Fluid Flows with Phase Change, Journal of Computational  
453 Physics 160 (2) (2000) 662 – 682.
- 454 [9] S. W. Welch, Local simulation of two-phase flows including interface tracking with mass transfer, Journal of Computational  
455 Physics 121 (1) (1995) 142 – 154.
- 456 [10] Y. Sato, B. Nieno, A sharp-interface phase change model for a mass-conservative interface tracking method, Journal of  
457 Computational Physics 249 (2013) 127 – 161.
- 458 [11] S. Hardt, F. Wondra, Evaporation model for interfacial flows based on a continuum-field representation of the source  
459 terms, Journal of Computational Physics 227 (11) (2008) 5871 – 5895.
- 460 [12] S. Tanguy, T. Ménard, A. Berlemont, A level set method for vaporizing two-phase flows, Journal of Computational Physics  
461 221 (2) (2007) 837 – 853.
- 462 [13] J. Schlottkke, B. Weigand, Direct numerical simulation of evaporating droplets, Journal of Computational Physics 227 (10)  
463 (2008) 5215 – 5237.
- 464 [14] J. Lee, G. Son, H. Y. Yoon, Numerical simulation of the quenching process in liquid jet impingement, International  
465 Communications in Heat and Mass Transfer 61 (2015) 146 – 152.
- 466 [15] M. Yazdani, T. Radcliff, M. Soteriou, A. A. Alahyari, A high-fidelity approach towards simulation of pool boiling, Physics  
467 of Fluids 28 (1) (2016) 012111.
- 468 [16] V. Mihalef, B. Unlusu, D. Metaxas, M. Sussman, M. Y. Hussaini, Physics based boiling simulation, in: Proceedings  
469 of the 2006 ACM SIGGRAPH/Eurographics Symposium on Computer Animation, SCA '06, Eurographics Association,  
470 Aire-la-Ville, Switzerland, Switzerland, 2006, pp. 317–324.
- 471 [17] L. Anumolu, M. F. Trujillo, Gradient augmented level set method for phase change simulations, Journal of Computational  
472 Physics 353 (2018) 377 – 406.
- 473 [18] H. Chen, C. Min, F. Gibou, A numerical scheme for the Stefan problem on adaptive Cartesian grids with supralinear  
474 convergence rate, Journal of Computational Physics 228 (16) (2009) 5803 – 5818.
- 475 [19] C. R. Kharangate, I. Mudawar, Review of computational studies on boiling and condensation, International Journal of  
476 Heat and Mass Transfer 108, Part A (2017) 1164 – 1196.
- 477 [20] J. Liu, C. M. Landis, H. Gomez, T. J. Hughes, Liquid-vapor phase transition: Thermomechanical theory, entropy stable  
478 numerical formulation, and boiling simulations, Computer Methods in Applied Mechanics and Engineering 297 (2015) 476  
479 – 553.

- 480 [21] J. Bueno, H. Gomez, Liquid-vapor transformations with surfactants. Phase-field model and Isogeometric Analysis , Journal  
481 of Computational Physics 321 (2016) 797 – 818.
- 482 [22] J. Bueno, C. Bona-Casas, Y. Bazilevs, H. Gomez, Interaction of complex fluids and solids: theory, algorithms and  
483 application to phase-change-driven implosion, Computational Mechanics 55 (6) (2015) 1105–1118.
- 484 [23] R. Saurel, R. Abgrall, A Multiphase Godunov Method for Compressible Multifluid and Multiphase Flows, Journal of  
485 Computational Physics 150 (2) (1999) 425 – 467.
- 486 [24] R. Saurel, F. Petitpas, R. Abgrall, Modelling phase transition in metastable liquids: application to cavitating and flashing  
487 flows, Journal of Fluid Mechanics 607 (2008) 313350.
- 488 [25] M. Khalloufi, Y. Mesri, R. Valette, E. Massoni, E. Hachem, High fidelity anisotropic adaptive variational multiscale  
489 method for multiphase flows with surface tension, Computer Methods in Applied Mechanics and Engineering 307 (2016)  
490 44 – 67.
- 491 [26] L. Marioni, M. Khalloufi, F. Bay, E. Hachem, Two-fluid flow under the constraint of external magnetic field: revisiting  
492 the dam-break benchmark, International Journal of Numerical Methods for Heat and Fluid Flow 29 (2016) 1–17.
- 493 [27] R. Valette, E. Hachem, M. Khalloufi, A. Pereira, M. Mackley, S. Butler, The effect of viscosity, yield stress, and surface  
494 tension on the deformation and breakup profiles of fluid filaments stretched at very high velocities, Journal of Non-  
495 Newtonian Fluid Mechanics 263 (2019) 130 – 139.
- 496 [28] C. Bahbah, M. Khalloufi, A. Larcher, Y. Mesri, T. Coupez, R. Valette, E. Hachem, Conservative and adaptive level-set  
497 method for the simulation of two-fluid flows, Computers & Fluids 191 (2019) 104223.
- 498 [29] E. Hachem, M. Khalloufi, J. Bruchon, R. Valette, Y. Mesri, Unified adaptive Variational MultiScale method for two phase  
499 compressible-incompressible flows , Computer Methods in Applied Mechanics and Engineering 308 (2016) 238 – 255.
- 500 [30] S. Riber, R. Valette, Y. Mesri, E. Hachem, Adaptive variational multiscale method for bingham flows, Computers & Fluids  
501 138 (2016) 51 – 60.
- 502 [31] Y. Mesri, M. Khalloufi, E. Hachem, On optimal simplicial 3D meshes for minimizing the Hessian-based errors , Applied  
503 Numerical Mathematics 109 (2016) 235 – 249.
- 504 [32] T. Coupez, Metric construction by length distribution tensor and edge based error for anisotropic adaptive meshing,  
505 Journal of Computational Physics 230 (7) (2011) 2391–2405.
- 506 [33] J. Sari, F. Cremonesi, M. Khalloufi, F. Cauneau, P. Meliga, Y. Mesri, E. Hachem, Anisotropic adaptive stabilized finite  
507 element solver for RANS models, International Journal for Numerical Methods in Fluids 86 (11) (2018) 717–736.
- 508 [34] S. Osher, R. Fedkiw, Level set methods and dynamic implicit surfaces, Springer, 2003.
- 509 [35] M. Sussman, P. Smereka, S. Osher, A level set approach for computing solutions to incompressible two-phase flow, Journal  
510 of Computational Physics 114 (1) (1994) 146 – 159.
- 511 [36] R. Denis, Modelisation and simulation of Leidenfrost effect in micro-droplets, Phd thesis, Université de Grenoble (Nov.  
512 2012).
- 513 [37] M. S. Lee, A. Riaz, V. Aute, Direct numerical simulation of incompressible multiphase flow with phase change, Journal  
514 of Computational Physics 344 (2017) 381 – 418.
- 515 [38] J. Brackbill, D. Kothe, C. Zemach, A continuum method for modeling surface tension, Journal of Computational Physics  
516 100 (2) (1992) 335 – 354.
- 517 [39] S. Hysing, A new implicit surface tension implementation for interfacial flows, International Journal for Numerical Methods  
518 in Fluids 51 (6) (2006) 659–672.
- 519 [40] G. C. Buscaglia, R. F. Ausas, Variational formulations for surface tension, capillarity and wetting, Computer Methods in  
520 Applied Mechanics and Engineering 200 (45 - 46) (2011) 3011 – 3025.
- 521 [41] V. Karyofylli, M. Frings, S. Elgeti, M. Behr, Simplex space-time meshes in two-phase flow simulations, International  
522 Journal for Numerical Methods in Fluids 86 (3) (2018) 218–230.

- 523 [42] T. Hughes, Multiscale phenomena: Green's functions, the Dirichlet-to-Neumann formulation, subgrid scale models, bubbles  
524 and the origins of stabilized methods , *Computer Methods in Applied Mechanics and Engineering* 127 (1 - 4) (1995) 387  
525 – 401.
- 526 [43] T. Hughes, G. R. Feijo, L. Mazzei, J.-B. Quincy, The variational multiscale method-a paradigm for computational me-  
527 chanics, *Computer Methods in Applied Mechanics and Engineering* 166 (1 - 2) (1998) 3 – 24.
- 528 [44] K. Nakshatrala, D. Turner, K. Hjelmstad, A. Masud, A stabilized mixed finite element method for darcy flow based on a  
529 multiscale decomposition of the solution, *Computer Methods in Applied Mechanics and Engineering* 195 (33 - 36) (2006)  
530 4036 – 4049.
- 531 [45] G. Scovazzi, Lagrangian shock hydrodynamics on tetrahedral meshes: A stable and accurate variational multiscale ap-  
532 proach, *Journal of Computational Physics* 231 (24) (2012) 8029 – 8069.
- 533 [46] U. Rasthofer, V. Gravemeier, Multifractal subgrid-scale modeling within a variational multiscale method for large-eddy  
534 simulation of turbulent flow, *Journal of Computational Physics* 234 (2013) 79 – 107.
- 535 [47] E. Castillo, R. Codina, Variational multi-scale stabilized formulations for the stationary three-field incompressible vis-  
536 coelastic flow problem, *Computer Methods in Applied Mechanics and Engineering* 279 (2014) 579 – 605.
- 537 [48] E. Hachem, B. Rivaux, T. Kloczko, H. Dignonnet, T. Coupez, Stabilized finite element method for incompressible flows  
538 with high reynolds number, *Journal of Computational Physics* 229 (23) (2010) 8643–8665.
- 539 [49] L. Formaggia, S. Perotto, Anisotropic error estimates for elliptic problems, *Numerische Mathematik* 94 (1) (2003) 67–92.
- 540 [50] J. Hoffman, C. Johnson, Adaptive finite element methods for incompressible fluid flow, *Error Estimation and Adaptive*  
541 *Discretization in Computational Fluid Dynamics* (Ed. T. J. Barth and H. Deconinck), *Lecture Notes in Computational*  
542 *Science and Engineering Vol.25*, Springer-Verlag Publishing, Heidelberg, 2003.
- 543 [51] G. Legrain, N. Moës, Adaptive anisotropic integration scheme for high-order fictitious domain methods: Application to  
544 thin structures, *International Journal for Numerical Methods in Engineering* 114 (8) (2018) 882–904.
- 545 [52] G. Kunert, R. Verfürth, Edge residuals dominate a posteriori error estimates for linear finite element methods on anisotropic  
546 triangular and tetrahedral meshes, *Numer. Math.* 86 (2) (2000) 283–303.
- 547 [53] F. Gibou, L. Chen, D. Nguyen, S. Banerjee, A level set based sharp interface method for the multiphase incompressible  
548 Navier-Stokes equations with phase change, *Journal of Computational Physics* 222 (2) (2007) 536 – 555.
- 549 [54] M. W. Akhtar, S. J. Kleis, Boiling flow simulations on adaptive octree grids, *International Journal of Multiphase Flow* 53  
550 (2013) 88 – 99.
- 551 [55] P. J. Berenson, Film-Boiling Heat Transfer From a Horizontal Surface, *Journal of Heat Transfer* 83 (3) (1961) 351 – 356.
- 552 [56] V. Klimenko, Film boiling on a horizontal plate - new correlation, *International Journal of Heat and Mass Transfer* 24 (1)  
553 (1981) 69 – 79.